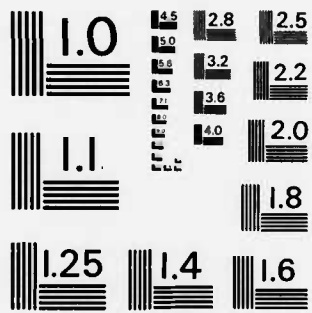


AD-A132 259 DEVELOPMENT OF A TECHNIQUE FOR SHORT-TERM PREDICTION OF 1/1
HYDROMETEORS USIN..(U) PENNSYLVANIA STATE UNIV
UNIVERSITY PARK DEPT OF METEOROLOGY G S FORBES ET AL.

UNCLASSIFIED MAR 83 SCIENTIFIC-1 AFGL-TR-83-0082 F/G 4/2 NL



END
DATE
FILED
•9 - 83
DTIC



MICROCOPY RESOLUTION TEST CHART
NATIONAL BUREAU OF STANDARDS - 1963 - A

AFGL-TR-83-0082

DEVELOPMENT OF A TECHNIQUE FOR SHORT-TERM
PREDICTION OF HYDROMETEORS USING
ADVECTION AND PHYSICAL FORCING

Gregory S. Forbes
John J. Cahir
Paul B. Dorian
Walter D. Lottes
Kathy Chapman

Department of Meteorology
The Pennsylvania State University
University Park, PA 16802

ADA132259

Scientific Report No. 1

March 1983

Approved for public release; distribution unlimited

AIR FORCE GEOPHYSICS LABORATORY
AIR FORCE SYSTEMS COMMAND
UNITED STATES AIR FORCE
HANSOM AFB, MASSACHUSETTS 01731

DTIC FILE COPY

DTIC
SELECTED
SEP 9 1983
S D

83 09 08 016

This report has been reviewed by the ESD Public Affairs Office (PA) and is releasable to the National Technical Information Service (NTIS).

This technical report has been reviewed and is approved for publication

H. Stuart Muench
H. STUART MUENCH
Contract Manager

Donald A. Chisholm
DONALD A. CHISHOLM, Chief
Atmospheric Prediction Branch

FOR THE COMMANDER

Robert A. McClatchey
ROBERT A. MCCLATCHY, Director
Meteorology Division

Qualified requestors may obtain additional copies from the Defense Technical Information Center. All others should apply to the National Technical Information Service.

If your address has changed, or if you wish to be removed from the mailing list, or if the addressee is no longer employed by your organization, please notify AFGL/DAA, Hanscom AFB, MA 01731. This will assist us in maintaining a current mailing list.

Do not return copies of this report unless contractual obligations or notices on a specific document requires that it be returned.

Unclassified

SECURITY CLASSIFICATION OF THIS PAGE (When Data Entered)

REPORT DOCUMENTATION PAGE		READ INSTRUCTIONS BEFORE COMPLETING FORM
1. REPORT NUMBER AFGL-TR-83-0082	2. GOVT ACCESSION NO. AD-A132 259	3. RECIPIENT'S CATALOG NUMBER
4. TITLE (and Subtitle) DEVELOPMENT OF A TECHNIQUE FOR SHORT-TERM PREDICTION OF HYDROMETEORS USING ADVECTION AND PHYSICAL FORCING		5. TYPE OF REPORT & PERIOD COVERED Scientific Report No. 1
7. AUTHOR(s) Gregory S. Forbes, John J. Cahir, Paul B. Dorian Walter D. Lottes, and Kathy Chapman	6. PERFORMING ORG. REPORT NUMBER F19628-82-K-0023	
9. PERFORMING ORGANIZATION NAME AND ADDRESS Department of Meteorology The Pennsylvania State University University Park, PA 16802	10. PROGRAM ELEMENT, PROJECT, TASK AREA & WORK UNIT NUMBERS 62101F 667010BB	
11. CONTROLLING OFFICE NAME AND ADDRESS Air Force Geophysics Laboratory Hanscom AFB, Massachusetts 01731 Monitor/H. Stuart Muench/LYP	12. REPORT DATE March 1983	
14. MONITORING AGENCY NAME & ADDRESS (if different from Controlling Office)	13. NUMBER OF PAGES 78	
15. SECURITY CLASS. (of this report) Unclassified		
15a. DECLASSIFICATION/DOWNGRADING SCHEDULE		
16. DISTRIBUTION STATEMENT (of this Report) Approved for public release; distribution unlimited		
17. DISTRIBUTION STATEMENT (of the abstract entered in Block 20, if different from Report)		
18. SUPPLEMENTARY NOTES		
19. KEY WORDS (Continue on reverse side if necessary and identify by block number) LFM humidity forecasts Satellite data processing Correlation studies Cloudiness forecasting		
20. ABSTRACT (Continue on reverse side if necessary and identify by block number) This interim scientific report describes initial stages of a project to enable prediction of humidity and cloudiness in mesoscale areas and their short-term changes. The performance of the LFM-II humidity forecasts is evaluated as an indicator of large-scale humidity patterns and their changes. The usefulness of various meteorological parameters as potential predictors of cloudiness and cloudiness change is assessed through correlation studies. The predictor fields are compared to brightness and brightness change fields		

derived from satellite imagery. Interactive computer programs to obtain quantitative data from satellite imagery are described. The ability of a humidity estimation technique, using hourly surface weather observations, to diagnose radiosonde-derived humidity observations is evaluated. Experiments in forecasting nighttime convection are described.

Accession For	
NTIS GRA&I	<input checked="" type="checkbox"/>
DTIC TAB	<input type="checkbox"/>
Unannounced	<input type="checkbox"/>
Justification	
By	
Distribution/	
Availability Codes	
Avail and/or	
Dist	Special
A	



Unclassified

Table of Contents

	Page
1. OVERVIEW -- NATURE OF PROCESSES WHICH AFFECT CLOUDINESS	1
2. LARGE-SCALE HUMIDITY CHANGE	3
2.1 Accuracy of LFM-II humidity forecasts for points	4
2.2 Estimation of layer humidities between radiosonde launches and on sub-synoptic scales	24
2.3. Accuracy of patterns of LFM-II humidity forecasts	29
3. DEVELOPMENT OF SATELLITE IMAGE-PROCESSING CAPABILITY	31
3.1 Overlay capabilities for interactive comparison of spatial relations between cloudiness and potential predictor fields	32
3.2 Quantitative processing of imagery statistics	36
3.3 Comparison of brightness and sub-synoptic scale, off-time simulated mean relative humidity	39
3.4 Comparison of brightness and LFM-II humidity forecasts	42
4. LOCAL FORCINGS AND INSTABILITIES	46
4.1 Studies of potential predictors	46
4.2 Studies of surface moisture convergence and cloudiness	50
4.3 Studies of precipitation and clouds along front-like boundaries	54
4.4 Polar vortices as responses to flow instabilities	63
5. INTRA-SYSTEM FEEDBACKS	63
6. PROSPECTUS FOR CONTINUED RESEARCH	68
Acknowledgements	70
References	71

List of Figures

Figure 1 Layers used in the study of LFM-II forecasts of relative humidity. A composite humidity profile is superimposed, with average values indicated for these layers: 50 mb boundary layer; top of PBL to 700 mb layer; 700-699 mb layer; 700-500 mb layer; 500-467 mb layer; 467-432 mb layer.

Figure 2 Photograph of the Grinnell television display of the visible satellite image at 1631 GMT on 3 September 1982. The box is movable by a cursor and is used for geographic registration of the image.

Figure 3 Photograph of the Grinnell television display of the visible satellite image of 1831 GMT on 28 August 1982 with an overlay of surface moisture divergence.

Figure 4 Average brightness of the satellite image of Fig. 3, calculated on 30x40 grid and displayed on a map.

Figure 5 Photograph of the Grinnell television display of the visible satellite image of 1631 GMT on 3 September 1982, with an overlay of average brightness, with averaging radius 128 km.

Figure 6a Minicomputer analysis of brightness (128 km averaging radius) at 1831 GMT on 24 August 1982.

Figure 6b Minicomputer analysis of simulated mean relative humidity at 1800 GMT on 24 August 1982.

Figure 7 Mapping of the absolute value of the gradient of the gradient of surface wet bulb potential temperature, the objective front locator parameter, at 0000 GMT on 16 August 1982. Also shown are locations of fronts analyzed by the National Meteorological Center.

Figure 8 Minicomputer analysis of the surface moisture divergence (in units of $10^{-5} \text{ g kg}^{-1} \text{ sec}^{-1}$) at 0000 GMT on 16 August 1982.

Figure 9 Display of the region where criteria are met satisfying the objective convection forecast parameter, TRW.

Figure 10 Schematic mapping of the mesoscale region of expected deep showers associated with surface moisture convergence near a front.

Figure 11 Schematic diagram showing the nature of the weather patterns conducive to nocturnal activated anafronts. At top is a horizontal mapping and at bottom a cross-section through the points indicated above.

Summary

The objective of this research is improved prediction, over the 3-15 h time range, of the patterns of cloudiness on synoptic and mesoscales that are seen in satellite imagery. Toward that end, work in progress includes studies in which the object is the atmospheric humidity in various layers, or the reflected brightness in satellite imagery. The emphasis is on the physical phenomena that can change the humidity or brightness and hence cloudiness, but it is recognized that persistence-climatology is often the best choice. These studies seek to identify situations when persistence climatology can be improved upon.

On synoptic scales, and over time periods of order 10 h, horizontal advection and large scale vertical motion introduce large changes in the humidity. It is found that a current operational moist model (LFM II) has good skill for the task of estimating these fields in all seasons, but has biases which change with time, and which vary vertically. In particular, the low-cloud-related layers in LFM II exhibit large positive initial humidity biases, which decrease with time; the middle-cloud related layer has an initial dry bias, which rapidly becomes positive and increases with time. Application of these predictions to cloudiness and cloudiness-change related to large-scale advection and vertical motion appears to be promising, but requires care.

Early results of studies of brightness change on satellite imagery suggest that attention must be given to flow regime and season. Physical forcing produces different outcomes in different conditions. Statistical statements can be misleading in such circumstances. However, it appears to be possible to quantify significant physical factors (on a scale consistent with a 1200 point mesh on the eastern 2/3 of the United States) in at least some flow regimes.

Detailed studies of important convective phenomena along boundaries and over relatively unstable surface layers are discussed and are continuing. It appears to be promising to extract measures of low-level temperature gradient, vorticity, stability and moisture convergence and to combine them in various ways to locate persisting or growing mesoscale cloud/precipitation patterns as a way to isolate regions where persistence-climatology can be improved on.

It is expected that forecasting guides or decision-trees related to the atmospheric humidity can be developed for these types of situations.

1. OVERVIEW — NATURE OF PROCESSES WHICH AFFECT CLOUDINESS

The objective of this research project is to develop a scheme (or schemes) for short-term forecasting of hydrometeors; i.e., clouds and precipitation. To a laboratory physicist the development of clouds and precipitation is conceptually and experimentally simple; readily accomplished through controlled cooling of moist air. For the practicing meteorologist, however, the forecasting of clouds and precipitation is made quite difficult because of the number of ways the atmosphere can achieve the required cooling and by the ability of atmospheric processes to alter the prevailing vapor content of the air. From a broad perspective, then, the challenge of this research (and of weather forecasting, in general) is to render a diversity of atmospheric processes into a format analogous to a controlled experiment. Just as a chemist knows that a certain combination of ingredients will react to produce a particular new substance, the forecaster needs to know the combination of conditions that results in clouds, or rain, or clearing.

In attempting to render the generalized problem of weather forecasting more tractable, historically there have been breakthroughs achieved through a number of techniques. Certainly one breakthrough was the recognition that much weather is produced by organized systems that translate, and forecast gains were made through use of the concepts of steering and wave propagation. A logical subsequent breakthrough was the recognition that weather systems were not steady, but evolved in response to (a) localized forcings or instabilities which were often geographic, topographic, or diurnal in nature and affected portions of the system, or (b) inherent instabilities of the environment on a scale larger than the system and affecting the entire system, or (c) feedbacks induced between various elements of the evolving weather system affecting either portions of the system or the system as a whole. Finally, just as the

chemist has formulae for reactions, numerical models solve formulae of the atmosphere to predict the end product of its combination of ingredients.

These historical breakthroughs have had the most impact on our ability to forecast meteorological quantities which are characteristic of synoptic scales and of a considerable depth of the atmosphere such as sea-level pressures, heights of the pressure surfaces, and (to a lesser extent) layer relative humidities. Much progress remains to be achieved in our ability to forecast cloudiness and precipitation, especially over short time periods and mesoscale areas.

The methodology of this hydrometeor-forecasting research project follows the historical examples cited above with respect to weather systems. Many clouds are associated with organized weather systems translating in a nearly steady state; the cloud patterns largely move with the system. Superimposed upon this translation are large-scale system changes, localized forcings or instabilities, and intra-system feedbacks. Initial stages of the research must address each of these aspects somewhat separately, and incorporation of the effects into a unified scheme must follow as a later stage. This interim report deals with accomplishments to date in the initial stages of the research plan.

In a broad sense the report treats the aspects of the forecast problem in this sequence: large-scale changes, local forcings and instabilities, and intra-system feedbacks. Interjected between these sections is a chapter on satellite image-processing capabilities developed as a tool for completing the research. Chapter 2 summarizes studies of large-scale humidity changes and their prediction using the LFM-II model. Chapter 3 discusses the development of the image-processing system and its use in relating the broad patterns of satellite-derived brightness to large-scale humidity analyses and forecasts.

Chapter 4 summarizes initial attempts to relate local forcings and instabilities to changes in cloud systems. Chapter 5 describes pilot studies to explore intra-system feedbacks (in which diabatic processes, advections, system slope, and system translation play key roles). Chapter 6 discusses the incorporation of these individual approaches into a coherent scheme.

2. LARGE-SCALE HUMIDITY CHANGE

One of the ways that cloudiness can change at a location is through propagation and change of cloud systems of synoptic scale. Current operational numerical models of the atmosphere are reasonably accurate in predicting the movement and changes in the accompanying synoptic-scale weather systems in terms of large-scale advections and vertical velocities. The object of this chapter is to assess the accuracy of an operational numerical model, the LFM-II, in forecasting layer relative humidities. Such forecasts can play an important role in forecasts of cloudiness and cloudiness change resulting from synoptic-scale processes. A qualitative assessment of model strengths and weaknesses would suggest that humidity changes due to large-scale advection of air from differing source regions and from large-scale vertical motion are treated reasonably well, but that changes due to mesoscale and diurnal processes must be addressed by supplemental or alternative techniques. The first part of this section deals with that suggestion quantitatively.

In assessing the accuracy of the LFM-II humidity forecasts, a number of items must be addressed:

1. accuracy of point forecasts by forecast layer, by season, and by forecast period;
2. accuracy of humidity change forecasts;
3. systematic errors in humidity forecasts and in range of predicted values;

4. differences between successive model runs, including possible diurnal effects;
5. systematic errors identifiable by weather regime.

In what follows, all relative humidities are expressed with respect to liquid water.

2.1 Accuracy of LFM-II humidity forecasts for points

In order to evaluate the quality of LFM-II humidity forecasts, it is necessary to specify the true humidity values. For humidity forecasts valid at 0000 and 1200 GMT, and for 12-hour changes valid between those times, radiosonde humidities have been considered the true values. In order to evaluate humidity forecasts and changes for other times, a simulated 1000-500 mb layer has been devised based upon hourly observations of sky cover, cloud bases, present weather, and surface relative humidity. The accuracy of this simulated humidity, in comparison with radiosondes at 0000 and 1200 GMT, is addressed in section 2.2.

One problem with the use of LFM-II humidity forecasts is that they are for sigma layers, whose top and bottom pressures and depths vary from station to station. The troposphere in the LFM is divided into 4 layers: a 50 mb deep, surface-based planetary boundary layer (PBL), and three layers of equal pressure depth between the top of the PBL and the model tropopause. Only the lowest 3 layers contain moisture. Since the model tropopause level was not available for this study, a standard atmosphere tropopause level of about 235 mb was applied. The average surface (i.e., station) pressure in the study was about 981 mb.

To simplify the calculations, radiosonde humidities were calculated for "standard" meteorological layers and then adjusted insofar as possible to match

the average LFM layers. The "standard" meteorological layers were: (1) 50 mb deep PBL (981 to 931 mb on average); (2) top of PBL to 700 mb; (3) 700 to 500 mb; (4) surface to 500 mb. These values were adjusted to approximate those of the average "LFM" layers: (1) 50 mb deep PBL (981 to 931 on average) to correspond to LFM boundary layer R_1 ; (2) layer 2 (931 to 699 mb on average) corresponds to LFM layer R_2 ; (3) layer 3 (699 to 467 mb on average) corresponds to LFM layer R_3 ; (4) mean layer (981 to 467 mb on average) corresponds to LFM layer MRH.¹ Figure 1 shows the various layers, and also the average initial-hour radiosonde humidity profile. The observed behavior of the humidity in these various layers was compared for a 40-case sample, involving about 2000 radiosonde soundings, with 10 cases in each season (Table 1).

Radiosonde layer humidities were calculated from significant level data in a pressure-weighted scheme. Standard layer humidities were adjusted to approximate the LFM layers via adjustment equations of the form:

$$\text{RH LFM layer} = a(\text{RAOB RH}) + b, \quad (1)$$

where a and b are constants determined from the differences in pressure levels of the layers and from the average relative humidities in the "misfit" layers. Formulation of the adjustment equations is presented in Table 2, using misfit-layer humidity values from the average radiosonde humidity profile of Fig. 1. Table 3 summarizes the correction constants used in Eq. (1) for various layer adjustments.

¹Additionally, a "different" layer was sometimes used in the calculation of the MRH layer. It was calculated from the surface to the first significant radiosonde level with a pressure equal to or less than 500 mb. This is referred to as "pseudo-MRH". On average, it included the layer from 981 to 432 mb. This pseudo-MRH layer is depicted in Figure 1.

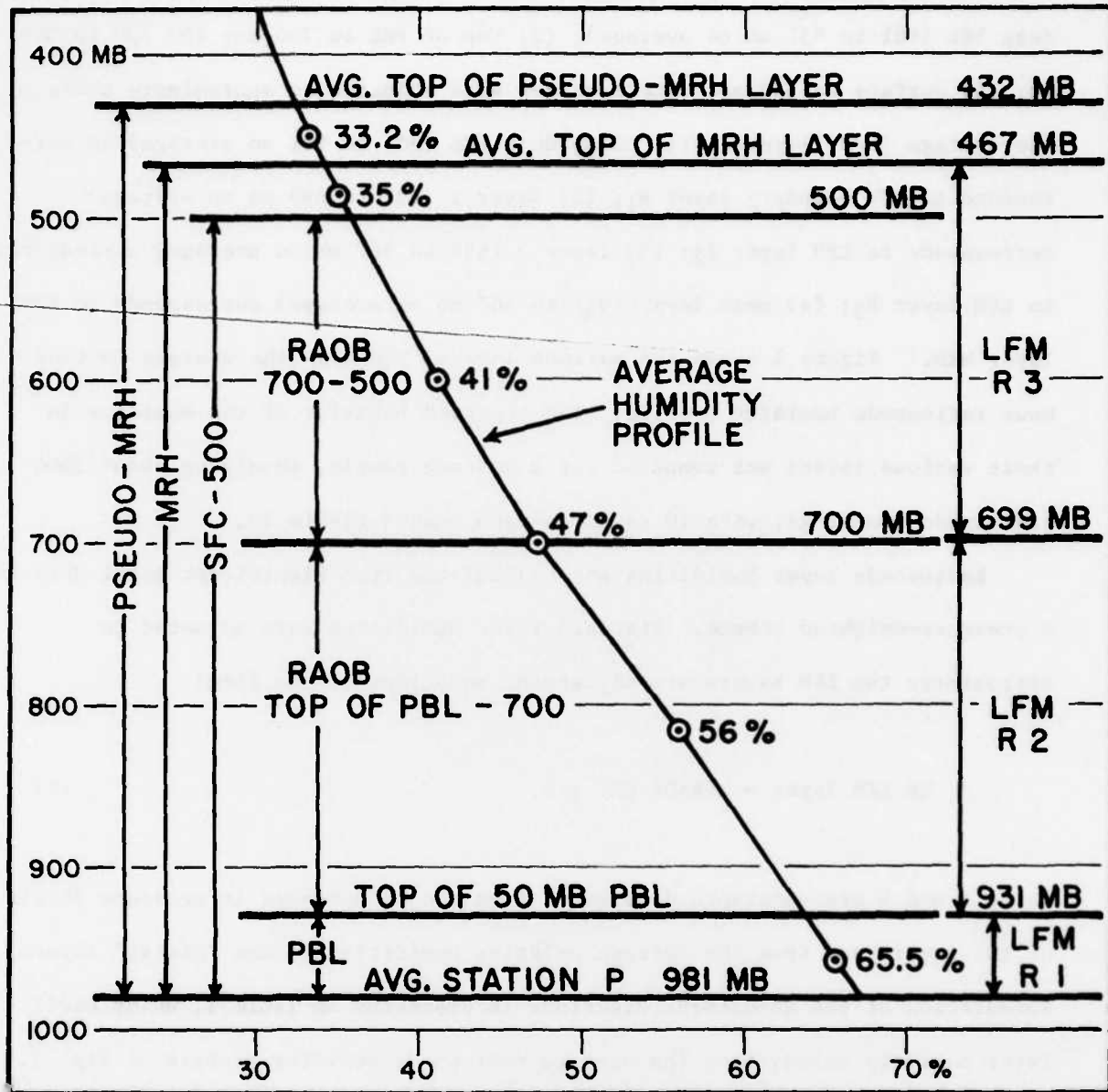


Figure 1

Layers used in the study of LFM-II forecasts of relative humidity. A composite humidity profile is superimposed, with average values indicated for these layers: 50 mb boundary layer; top of PBL to 700 mb layer; 700-699 mb layer; 700-500 mb layer; 500-467 mb layer; 467-432 mb layer.

Table 1
List of Cases

<u>Fall</u>		<u>Winter</u>
	<u>Sept./Oct. 1981</u>	<u>Dec. 1981/Jan. 1982</u>
10/08/81 - 10/09/81		12/05/81 - 12/06/81
10/11/81 - 10/12/81		12/07/81 - 12/08/81
10/15/81 - 10/16/81	00-00Z	12/10/81 - 12/11/81
10/30/81 - 10/31/81		01/02/82 - 01/03/82
09/23/81 - 09/24/81		01/05/82 - 01/06/82
10/20/81 - 10/21/81		12/09/81 - 12/10/81
10/23/81 - 10/24/81		01/14/82 - 01/15/82
09/12/81 - 09/13/81	12-12Z	01/17/82 - 01/18/82
09/17/81 - 09/18/81		12/25/81 - 12/26/81
09/08/81 - 09/09/81		12/29/81 - 12/30/81
<u>Spring</u>		<u>Summer</u>
	<u>March/April 1982</u>	<u>June/July 1981; July 1982</u>
03/07/82 - 03/08/82		06/07/81 - 06/08/81
04/07/82 - 04/08/82		06/25/81 - 06/26/81
04/10/82 - 04/11/82	00-00Z	06/28/81 - 06/29/81
03/24/82 - 03/25/82		07/03/81 - 07/04/81
03/29/82 - 03/30/82		07/13/81 - 07/14/81
03/11/82 - 03/12/82		07/08/82 - 07/09/82
04/01/82 - 04/02/82		07/10/82 - 07/11/82
04/15/82 - 04/16/82	12-12Z	07/21/82 - 07/22/82
04/18/82 - 04/19/82		07/25/82 - 07/26/82
04/13/82 - 04/14/82		06/03/81 - 06/04/81

Table 2

Method of Approximating LFM Layer Humidities
from Standard Layer Humidities

<u>LFM Layer</u>	<u>Standard Layer</u>
R_1	$\equiv R_1$
R_2	$\equiv \frac{231(\bar{R}^{PBL\ TOP-700}) + 1\bar{R}^{700-699}}{931-699}$
	$\equiv 0.996(\bar{R}^{PBL\ TOP-700}) + 0.2\%$
R_3	$\equiv \frac{200(\bar{R}^{700-500}) + 33(\bar{R}^{500-467}) - 1(\bar{R}^{700-699})}{699-467}$
	$\equiv 0.862(\bar{R}^{700-500}) + 4.78\%$
MRH	$\equiv \frac{50(R_1) + 231(\bar{R}^{PBL\ TOP-700}) + 200(\bar{R}^{700-500}) + 33(\bar{R}^{500-467})}{981-467}$
	$\equiv 0.097(R_1) + 0.449(\bar{R}^{PBL\ TOP-700}) + 0.389(\bar{R}^{700-500}) + 2.25\%$
	$\equiv \frac{481(\bar{R}^{SFC-500}) + 33(\bar{R}^{500-467})}{981-467}$
	$\equiv 0.936(\bar{R}^{SFC-500}) + 2.25\%$
Alternatively, from Pseudo-MRH layer	
MRH	$\equiv \frac{549(\bar{R}^{SFC-432}) - 35(\bar{R}^{467-432})}{981-467}$
	$\equiv 1.067(\bar{R}^{SFC-432}) - 2.24\%$

Table 3

Constant for Conversion from Standard Layers to LFM Layers

$$\text{LFM} = a(\text{RAOB}) + b$$

<u>Conversion</u>	<u>a</u>	<u>b</u>
R_1	1.000	0
$\bar{R} \text{ PBL TOP-700} \rightarrow R_2$	0.996	0.20%
$\bar{R} \text{ 700-500} \rightarrow R_3$	0.862	4.78%
$\bar{R} \text{ SFC-500} \rightarrow \text{MRH}$	0.936	2.25%
$\bar{R} \text{ SFC-432} \rightarrow \text{MRH}$	1.067	-2.24%

Table 4 represents values of the layer mean humidities and standard deviations for all radiosonde observations, by season and annually, for the various layers described above. These values are valid at times of LFM initial analyses. Several general observations can be made from Table 4:

1. Observed layer relative humidities decrease rather steadily with height, but are most variable aloft in all seasons except Spring. The differences between the "standard" layers and adjusted ("LFM") layers are not large.
2. Layer relative humidities are highest in summer in each layer.
3. In this sample, PBL humidity was lowest in spring, top of PBL-700 humidity was lowest in winter, and 700-500 humidity was lowest in fall; again, these statements hold for the adjusted layers, as well.
4. Standard deviations of the layer humidities ranged from 15 to 27%, tending to increase with height except in Spring, with the surface-500 mb layer showing smaller values than the other layers; in the adjusted upper layer, the standard deviations are of somewhat smaller magnitude. Also the adjustment produces an anomalous decrease upward in winter.
5. The humidities in the layers corresponding to the LFM R_3 and MRH and, the pseudo-MRH layer showed slightly lower humidities than the comparable "standard" layers. Standard deviations of the pseudo-MRH were somewhat larger than either the "standard" or "LFM" standard deviations.

LFM humidities were obtained directly from FOUS 60-78 transmissions over the FAA 604 circuit. The accuracy of LFM humidities was assessed using the 40-case sample of Table 1. This was a period during which the model physics apparently remained nearly constant. In most cases (except where otherwise

Table 4

Comparison of Initial-hour Rainsonde Humidities for Different Layers by season

"Standard" Layers (Calculated)			LFM Layers (adjusted from standard layers)			PSEUDO-MRH Layer (Calculated)		
Layer	Mean	S.D.	Layer	Mean	S.D.	Layer	Mean	S.D.
<u>FALL</u>			<u>FALL</u>			<u>FALL</u>		
Lowest 50 mb	66.9	19.3	R ₁	66.9	19.3			
Top of PBL -700	56.2	23.0	R ₂	56.2	22.9			
700-500	36.7	26.9	R ₃	36.4	25.0			
SFC-500	48.9	19.1	MRH	48.0	19.9	PSEUDO MRH	46.9	20.6
<u>WINTER</u>			<u>WINTER</u>			<u>WINTER</u>		
Lowest 50 mb	63.6	22.5	R ₁	63.6	22.5			
Top of PBL -700	51.2	24.3	R ₂	51.1	24.2			
700-500	39.5	25.1	R ₃	38.8	23.3			
SFC-500	47.4	18.2	MRH	46.6	19.5	PSEUDO MRH	46.1	20.2
<u>SPRING</u>			<u>SPRING</u>			<u>SPRING</u>		
Lowest 50 mb	62.7	23.4	R ₁	62.7	23.4			
Top of PBL -700	52.8	23.0	R ₂	52.7	22.9			
700-500	41.1	23.1	R ₃	40.2	21.4			
SFC-500	48.8	15.5	MRH	47.9	17.9	PSEUDO MRH	47.9	18.5
<u>SUMMER</u>			<u>SUMMER</u>			<u>SUMMER</u>		
Lowest 50 mb	68.5	19.9	R ₁	68.5	19.9			
Top of PBL -700	63.9	16.9	R ₂	63.9	16.9			
700-500	47.2	24.8	R ₃	45.4	23.0			
SFC-500	57.4	15.4	MRH	56.0	17.4	PSEUDO MRH	54.9	18.0
<u>ANNUAL</u>			<u>ANNUAL</u>			<u>ANNUAL</u>		
Lowest 50 mb	65.4	21.3	R ₁	65.4	21.3			
Top of PBL -700	56.0	21.9	R ₂	55.9	21.9			
700-500	41.1	25.0	R ₃	40.2	23.2			
SFC-500	50.6	17.1	MRH	49.6	18.7	PSEUDO MRH	49.0	19.4

noted), values of LFM humidity were interpolated from FOUS stations to the locations of radiosonde sites. (In a few experiments, described in a later section, both radiosonde and LFM values were interpolated to fixed grid points). All available radiosondes in the region east of the Rocky Mountain states were used when FOUS data were also available nearby. Half of the cases in each season corresponded to a 0000 GMT model cycle and half to a 1200 GMT cycle.

Table 5 presents LFM humidity forecasts at 6-hour forecast intervals. In the annual mean, the model PBL (R_1), layer 2 (R_2) and mean (MRH) humidities decrease rather steadily with time, whereas the layer 3 (R_3) humidities show a slow but steady increase. These model trends generally showed up in the seasonal means, most notably in Fall and Spring, though the trends were not as steady in some layers. The model standard deviations gave signs of a similar performance, though not nearly as steady.

The tendency for the two lowest layers to dry out with time while the upper moistens shows a changing bias. Table 6 compares means and standard deviations of LFM layer humidities (for the LFM layers) with those observed at analysis and forecast times. It can be seen that the model standard deviations are almost universally lower than those of the radiosonde data, though this may result from the smoothing effect of interpolation of LFM values to radiosonde sites. Of most importance, in the annual means the LFM shows considerable bias in some layers, and some trends in the bias. In layers 1 and 2, positive (moist) analysis biases transform to negative biases by 24 hours and often by 12 hours. Layer 3 displays an initial positive bias which grows with time. The mean relative humidity begins with a moist bias, which reduces slowly with time.

Table 5

LFM Humidity Values

	00 hr		06 hr		12 hr		18 hr		24 hr	
	Mean	S.D.								
FALL										
R ₁	77.9	17.6	70.4	17.5	69.5	15.4	63.9	17.4	62.4	15.8
R ₂	60.8	20.8	56.8	20.4	54.4	18.0	53.4	20.1	51.8	17.7
R ₃	38.5	18.6	39.4	22.8	39.0	20.8	39.6	25.6	41.7	20.6
MRH	57.1	17.0	53.8	17.1	51.7	15.5	50.8	17.6	49.9	15.4
WINTER										
R ₁	73.6	19.3	69.4	21.9	65.4	19.1	63.7	21.0	60.8	18.4
R ₂	58.7	22.5	58.1	24.2	51.2	19.9	52.9	24.0	50.4	19.3
R ₃	46.2	18.9	44.7	24.9	44.3	21.6	47.2	27.1	49.5	22.2
MRH	56.2	18.8	54.9	21.7	50.4	17.7	52.2	20.9	50.4	16.2
SPRING										
R ₁	72.3	18.6	67.2	19.3	66.2	17.6	63.2	19.3	61.8	17.6
R ₂	58.7	19.5	55.4	19.9	52.5	18.5	53.5	22.1	51.1	18.5
R ₃	43.7	15.3	46.6	23.6	48.7	20.6	47.8	26.8	51.1	22.8
MRH	56.7	15.4	54.4	17.4	53.4	16.1	52.9	19.4	52.4	16.1
SUMMER										
R ₁	79.1	18.8	71.3	17.7	72.2	12.0	67.3	17.1	62.9	16.3
R ₂	70.6	14.9	64.6	13.6	64.3	11.0	62.3	15.3	58.8	12.7
R ₃	44.4	16.3	49.3	20.2	50.9	19.1	51.2	23.3	48.5	18.8
MRH	65.0	13.2	61.6	13.1	62.0	11.3	60.0	15.6	56.5	12.2
ANNUAL										
R ₁	75.7	18.6	69.6	19.2	68.3	16.2	64.5	18.8	62.0	17.1
R ₂	62.2	19.6	58.7	19.9	55.6	17.2	55.5	20.6	53.0	17.2
R ₃	43.2	17.3	45.0	22.9	45.7	20.5	46.5	25.7	47.7	21.2
MRH	58.7	16.2	56.2	17.6	54.4	15.3	54.0	18.5	52.3	15.0

Table 6
Comparison of LFM & RAOB

	00 hr LFM/RAOB		12 hr LFM/RAOB		24 hr LFM/RAOB	
	Mean	S.D.	Mean	S.D.	Mean	S.D.
FALL						
R ₁	77.9/66.9	17.6/19.3	69.5/68.2	15.4/20.5	62.4/66.2	15.8/17.0
R ₂	60.8/56.2	20.8/22.9	54.4/54.6	18.0/22.5	51.8/54.3	17.7/22.8
R ₃	38.5/36.4	18.6/25.0	39.0/33.0	20.8/23.1	41.7/32.7	20.6/22.5
MRH	57.1/48.0	17.0/19.9	51.7/46.1	15.5/18.3	49.9/45.7	15.4/18.4
WINTER						
R ₁	73.6/63.6	19.3/22.5	65.4/62.0	19.1/21.6	60.8/63.4	18.4/21.2
R ₂	58.7/51.1	22.5/24.2	51.2/47.4	19.9/23.5	50.4/48.6	19.3/23.0
R ₃	46.2/38.8	18.9/23.3	44.3/37.0	21.6/21.6	49.5/39.3	22.2/21.5
MRH	56.2/46.6	18.8/19.5	50.4/44.2	17.7/18.9	50.4/45.8	16.2/17.6
SPRING						
R ₁	72.3/62.7	18.6/23.4	66.2/60.8	17.6/23.1	61.8/64.5	17.6/25.2
R ₂	58.7/52.7	19.5/22.9	52.5/52.8	18.5/23.2	51.1/52.8	18.5/22.4
R ₃	43.7/40.2	15.3/21.4	48.7/41.5	20.6/21.9	51.1/40.3	22.8/21.9
MRH	56.7/47.9	15.4/17.9	53.4/48.7	16.1/17.6	52.4/48.5	16.1/17.5
SUMMER						
R ₁	79.1/68.5	18.8/19.9	72.2/71.4	12.0/17.1	62.9/68.9	16.3/19.3
R ₂	70.6/63.9	14.9/16.9	64.3/64.7	11.0/16.6	58.5/64.0	12.7/16.5
R ₃	44.4/45.4	16.3/23.0	50.9/45.4	19.1/23.6	48.5/46.5	18.8/22.0
MRH	65.0/56.0	13.2/17.4	62.0/56.7	11.3/17.6	56.5/56.7	12.2/17.0
ANNUAL						
R ₁	75.7/65.4	18.6/21.3	68.3/65.6	16.2/20.6	62.0/65.7	17.1/20.9
R ₂	62.2/55.9	19.6/21.9	55.6/54.8	17.2/21.6	53.0/54.9	17.2/21.3
R ₃	43.2/40.2	17.3/23.2	45.7/39.2	20.5/22.5	47.7/39.7	21.2/22.0
MRH	58.7/49.6	16.2/18.7	54.4/48.9	15.3/18.1	52.3/49.1	15.0/17.6

Table 7 displays these biases (mean errors) and also presents a measure of the absolute accuracy of an individual forecast, the root mean square error. The rms errors ranged from 13 to 24%, and represented contributions from both systematic and random error. The rms errors were generally smallest in layer 2. Table 8 presents similar results, except the LFM forecasts have been compared to standard layers. Differences in values between Tables 7 and 8 are slight.

Table 9 presents rms errors of LFM forecasts after removal of the biases presented in Table 7. Trends in the errors begin to appear, indicating that the random error generally grows slowly with time as expected a priori. Of interest are the exceptions to this expectation:

1. the rms errors are greatest in layer 1 at 12 hours in each season, suggesting an inability of the model to handle the spatial patterns in diurnal boundary layer processes;
2. the largest rms error of all shows up in layer 3 in summer in the initial analysis, perhaps due to convective influences.
3. Substantial rms errors occur at the initial times, highlighting weaknesses in the analysis methods used.

Whereas Tables 8 and 9 provide a measure of the reliability of a humidity forecast at a point before and after bias removal, it is also of interest to inquire how variance of the model humidities affects the comparison of the relative accuracies of the various layer forecasts. Table 10 measures the rms errors before and after bias removal as fractions of the standard deviation of the layer humidity forecasts. Whereas Tables 8 and 9 suggest that layer 2 is overwhelmingly best, Table 10 indicates that the rms error in layer 3 is often a smaller percentage of the model variance, especially after 24 hours.

Table 7
Mean and RMS Errors of LFM Layers

	00 hr LFM-RAOB		12 hr LFM-RAOB		24 hr LFM-RAOB	
	Mean	RMS	Mean	RMS	Mean	RMS
<u>FALL</u>						
R ₁	11.0	15.4	1.3	20.3	-3.8	16.9
R ₂	4.7	13.4	-0.3	14.4	-2.6	17.0
R ₃	2.1	16.2	6.0	17.3	8.9	19.8
MRH	9.0	16.7	5.5	16.7	4.2	18.5
<u>WINTER</u>						
R ₁	10.1	15.3	3.3	16.8	-2.6	17.8
R ₂	7.5	12.8	3.7	12.6	1.7	15.8
R ₃	7.4	10.9	7.3	16.0	10.2	22.4
MRH	9.6	15.5	6.1	14.2	4.6	15.1
<u>SPRING</u>						
R ₁	9.6	16.1	5.3	19.5	-2.6	18.3
R ₂	5.9	14.3	-0.4	15.7	-1.8	17.6
R ₃	3.5	13.9	7.2	19.7	10.7	24.6
MRH	8.7	17.8	4.7	17.3	3.9	18.5
<u>SUMMER</u>						
R ₁	10.6	14.7	0.8	19.3	-6.0	18.4
R ₂	6.7	12.6	-0.4	11.7	-5.2	16.0
R ₃	-1.0	22.5	5.4	16.8	1.9	19.7
MRH	9.0	15.1	5.2	13.5	-0.3	14.0
<u>ANNUAL</u>						
R ₁	10.3	15.4	2.7	19.0	-3.8	17.8
R ₂	6.2	13.3	0.7	13.7	-2.0	16.6
R ₃	3.0	15.9	6.5	16.3	7.9	19.9
MRH	9.1	16.3	5.4	15.5	3.1	16.6

Table 8
Mean and RMS Errors of LFM Humidities as Estimates of "Standard" Layers

	00 hr LFM-RAOB		12 hr LFM-RAOB		24 hr LFM-RAOB	
	Mean	RMS	Mean	RMS	Mean	RMS
FALL						
Lowest 50 mb	11.0	15.4	1.3	20.3	-3.8	16.9
Top of PBL -700	4.5	13.5	-0.3	14.4	-2.6	17.1
700-500	1.7	18.6	6.2	19.1	9.2	21.5
SFC-500	7.9	16.8	4.9	17.0	3.3	18.8
WINTER						
Lowest 50 mb	10.1	15.3	3.3	16.8	-2.6	17.8
Top of PBL -700	7.5	12.8	3.7	12.6	1.7	15.9
700-500	6.7	15.7	6.9	16.9	9.3	21.1
SFC-500	8.8	14.9	5.6	13.9	3.8	15.0
SPRING						
Lowest 50 mb	9.6	16.1	5.3	19.5	-2.6	18.3
Top of PBL -700	5.9	14.3	-0.4	15.7	-1.8	17.7
700-500	2.6	15.9	6.1	19.8	9.8	24.0
SFC-500	8.0	17.5	4.1	17.1	3.1	18.6
SUMMER						
Lowest 50 mb	10.6	14.7	0.8	19.3	-6.0	18.4
Top of PBL -700	6.6	12.6	-0.5	11.8	-5.3	16.1
700-500	-2.8	17.6	3.7	18.4	0.1	21.6
SFC-500	7.5	14.3	3.7	13.1	-1.8	14.1
ANNUAL						
Lowest 50 mb	10.3	15.4	2.7	19.0	-3.8	17.8
Top of PBL -700	6.1	13.3	0.6	13.7	-2.0	16.7
700-500	2.1	17.0	5.7	18.6	7.1	22.1
SFC-500	8.1	15.9	4.6	15.4	2.1	16.8

Table 9
RMS Errors of LFM Layers after BIAS removed

	00 hr	12 hr	24 hr
<u>FALL</u>			
R ₁	10.8	20.2	16.5
R ₂	12.6	14.4	16.8
R ₃	16.1	16.3	17.7
MRH	14.0	15.7	18.0
<u>WINTER</u>			
R ₁	11.5	16.4	17.6
R ₂	10.3	12.0	15.7
R ₃	8.0	14.3	20.0
MRH	12.1	12.8	14.4
<u>SPRING</u>			
R ₁	12.9	18.8	18.1
R ₂	13.0	15.6	17.5
R ₃	13.4	18.3	22.1
MRH	15.5	16.6	18.1
<u>SUMMER</u>			
R ₁	10.2	19.3	17.4
R ₂	10.7	11.7	15.1
R ₃	22.5	15.9	19.6
MRH	12.2	12.5	13.9
<u>ANNUAL</u>			
R ₁	11.4	18.7	17.4
R ₂	11.7	13.7	16.3
R ₃	15.6	14.9	18.3
MRH	13.5	14.5	16.3

Table 10
Ratio of LFM RMSE to S.D. Before & After Bias Removal

	00 hr	12 hr	24 hr
<u>FALL</u>	Before/After	Before/After	Before/After
R ₁	0.88/0.61	1.32/1.31	1.07/1.04
R ₂	0.64/0.61	0.80/0.80	0.96/0.95
R ₃	0.87/0.87	0.83/0.78	0.96/0.86
MRH	0.98/0.82	0.99/1.01	1.20/1.17
<u>WINTER</u>	Before/After	Before/After	Before/After
R ₁	0.79/0.60	0.88/0.86	0.97/0.96
R ₂	0.57/0.46	0.63/0.60	0.82/0.81
R ₃	0.58/0.42	0.74/0.66	1.01/0.90
MRH	0.82/0.64	0.80/0.72	0.93/0.89
<u>SPRING</u>	Before/After	Before/After	Before/After
R ₁	0.87/0.69	1.11/1.07	1.04/1.03
R ₂	0.73/0.69	0.85/0.84	0.95/0.95
R ₃	0.91/0.88	0.96/0.89	1.08/0.97
MRH	1.61/1.01	1.07/1.03	1.15/1.12
<u>SUMMER</u>	Before/After	Before/After	Before/After
R ₁	0.78/0.54	1.61/1.61	1.13/1.07
R ₂	0.85/0.72	1.06/1.06	1.26/1.19
R ₃	1.38/1.38	0.88/0.83	1.05/1.04
MRH	1.14/0.92	1.19/1.11	1.15/1.14
<u>ANNUAL</u>	Before/After	Before/After	Before/After
R ₁	0.83/0.61	1.17/1.15	1.04/1.02
R ₂	0.68/0.60	0.80/0.80	0.97/0.95
R ₃	0.92/0.90	0.80/0.73	0.94/0.86
MRH	1.01/0.83	1.01/0.95	1.11/0.92

Table 11 presents, for pseudo-MRH only, comparison of humidities, standard deviations, mean errors, and rms errors at 0-24 hour forecast times for the 0000 and 1200 GMT forecast cycles.² Both cycles show the overall trend: the LFM begins with a large positive (moist) bias, which decreases with time. At 0 and 24 hours both forecast cycles have essentially the same mean errors. However, at 12 hours (midway through the atmosphere diurnal cycle) the two cycles show considerably different mean errors. Because the atmosphere is more moist at 1200 GMT (by about 3% in this layer) than at 0000 GMT, and because the 0000 GMT forecast cycle begins with a moist bias, the mean error in the 12-hour forecast (valid at 1200 GMT) is reduced. Because the atmosphere dries out between 1200 and 0000 GMT, and because the 1200 GMT cycle began with a moist bias, the 1200 GMT forecast cycle maintains a rather large moist bias in the 12-hour forecast (valid at 0000 GMT). There is definitely a small, systematic difference in 12-hr mean relative humidity forecasts between 0000 and 1200 GMT forecast cycles, apparently resulting from damped diurnal processes in the model, with the 1200 GMT cycle forecasts being comparatively more humid. This systematic difference is likely to affect other moisture-related quantities, although there may be opposing effects due to expected systematic errors in model static stability also resulting from damped diurnal processes.

Origins of other model errors are difficult to deduce without a series of sensitivity tests. From the present study, and a basic knowledge of the model and atmosphere, a few speculations are possible.

²These values were computed on a grid rather than at radiosonde sites, requiring interpolation of both LFM and radiosonde values. Tests of the effect of the extra interpolation showed that there was typically less than 1%, and never more than 2%, change of mean humidity, but about a 2% decrease in standard deviation.

Table 11

Comparison of 0000 and 1200 GMT Forecast Cycle
 LFM MRH with PSEUDO-MRH at Grid Points

	Annual Average 0000 GMT LFM/RAOB	Annual Average 1200 GMT LFM/RAOB
Initial-hour		
Mean	55.7/46.4	60.2/50.3
S.D.	14.8/15.3	14.9/15.6
Mean E	9.3	9.9
RMS E	12.4	13.0
06-hour		
Mean	54.3/NA	56.4/NA
S.D.	13.5/NA	14.0/NA
12-hour		
Mean	54.2/49.3	54.1/46.9
S.D.	14.1/15.4	14.8/15.7
Mean E	4.9	7.2
RMS E	10.8	12.0
18-hour		
Mean	53.4/NA	54.1/NA
S.D.	14.6/NA	14.7/NA
24-hour		
Mean	52.7/47.6	55.0/50.3
S.D.	15.5/15.6	14.5/15.2
Mean E	5.1	4.7
RMS E	11.9	11.2

- a. Initial biases. From Table 7 it can be seen that the initial bias is largest near the surface and decreases with height. The biases are not a constant percentage of the humidity, however, indicating that the problem is not one of application of an inflation factor. The use of only surface and mandatory level data probably contributes to the moist bias. Apparently the first guess field, the 12-hour humidity forecast from the spectral model, contributes to the bias at grid points away from radiosonde sites.
- b. MRH positive bias and small standard deviation. A smoothing function (G-Filter) is applied to the LFM MRH field and not to the individual three layers as a post-processing step at NMC. By inspection of Table 5, this appears to reduce the standard deviation of the MRH layer below that of any individual layer. Further, the pressure-weighted mean relative humidity calculated from the three layers does not match the MRH. In this sample, the G-filter appears to introduce a positive bias of 3-4%, the effect decreasing with time (as the model bias decreases) to about 1% by 24 hours.
- c. Layers 1 and 2 bias change. Beginning with large positive bias, layers 1 and 2 develop negative biases by 24 hours. This would appear to result from the absence of model surface evaporative fluxes over land perhaps in combination with excessive model vertical mixing associated with convective processes.
- d. Layer 3 bias change. This increase may result from excessive model mixing, perhaps associated with convective processes. Another contribution may arise from fictitious fluxes between layer 3 and 4,

which does not explicitly contain moisture. Humidity there is estimated for flux purposes, from linear extrapolation of layers 1-3. It is speculated that under subsidence conditions the true humidities in layer 4 would be anomalously dry, resulting in model estimates being too moist.

e. Other error sources. The effects of radiosonde movement and asynoptic launch times appears to be small. Convective processes during the summer season appeared to affect layer 3. The effect of model precipitation is to drain the atmosphere moisture supply, contributing to a temporal decline in the mean relative humidity. The effects of interpolation of the LFM data to radiosonde sites appears to significantly affect only the standard deviations. The effects of adjusting "standard" layers to match LFM layers appear to be small.

In summary, this study has shown that the LFM-II humidity forecasts contain considerable biases, which can be removed operationally to improve the forecasts. Ideally, bias statistics could be updated regularly to account for seasonal changes and alterations made to the model. Even after removal of the biases, the model appears unable to adequately forecast the PBL humidity at 12 hours except in winter, and rms errors in layer 3 are rather large at 24 hours except in the fall. In other instances, rms errors are in the 13-18% range. Obviously, the LFM-II humidity forecasts can show considerable errors at a given location. Additional study is needed to determine whether portions of these errors can be eliminated through recognition of biases related to weather regime (such as through erroneous forecasts of system speed, etc.).

2.2 Estimation of layer humidities between radiosonde launches and on sub-synoptic scales.

In order to assess the validity of humidity forecasts at times other than 0000 or 1200 GMT, some reliable technique for estimating the true humidity is needed. A program was developed a few years ago at Penn State for this purpose, utilizing hourly surface observations. The scheme is somewhat similar to one used at NMC, and has procedures similar to those in the conventional data processor of the automated cloud analysis model of the Air Force Global Weather Control (Fye, 1978). Basically, the program uses reports of cloud cover, cloud base, present weather, and surface relative humidity to produce a simulated 1000-500 mb mean relative humidity.

Table 12 presents the results of a comparison between the simulated-MRH and 4 calculated radiosonde layer values: surface to 500 mb layer; estimated MRH layer; pseudo-MRH layer calculated at radiosonde sites; pseudo MRH layer calculated at grid points. Overall, the simulated MRH is quite good, and best matches the pseudo MRH layer. Except during the summer, the simulated MRH shows mean error less than 2% in each season and for each layer. The simulated MRH really shows only two weaknesses. During the summer season the simulated MRH displays a moderately large negative (dry) bias. Second, the variance of the simulated humidities is considerably less than that of the real atmosphere.

Table 12 also presents rms errors of the simulated MRH values, in comparison with grid point values of pseudo MRH. Strictly this is the only proper comparison, as the simulated MRH values were calculated at grid points. The rms errors are rather satisfying; as small or smaller than those of LFM forecasts.

Table 13 presents seasonal and diurnal trends in the simulated MRH, in comparison with 0000 and 1200 GMT values of the pseudo-MRH calculated at grid

Table 12

Comparison of Simulated MRH to RAOB Values for
 Combined 0000 and 1200 GMT Observations
 (30 Observations per Season)

	Simulated MRH (Grid Pt.)	Calculated RAOB SFC-500	Estimated MRH	Calculated PSEUDO-MRH (RAOB Sites)	Calculated PSEUDO-MRH (Grid Pt.)
FALL					
Mean	45	47	47	45	45
S.D.	13	18	19	20	16
Mean E		-2	-2	0	-1
RMSE					12
WINTER					
Mean	47	46	46	45	46
S.D.	16	17	19	19	17
Mean E		+1	+1	+1	0
RMSE					13
SPRING					
Mean	49	49	48	48	48
S.D.	14	16	18	18	15
Mean E		0	+1	+1	0
RMSE					11
SUMMER					
Mean	49	58	56	55	55
S.D.	12	16	17	18	14
Mean E		-9	-7	-6	-6
RMSE					14
ANNUAL					
Mean	48	50	49	49	48
S.D.	14	17	18	19	16
Mean E		-2	-1	-1	0
RMSE					12

Table 13

**Season and Annual Averages of Diurnal Trends in
Simulated MRH in Comparison with
Grid Point Values of Pseudo MRH**

	Fall Sim/RAOB	Winter Sim/RAOB	Spring Sim/RAOB	Summer Sim/RAOB	Annual Sim/RAOB
0000 GMT					
Mean	46/44	47/44	49/48	49/52	48/47
S.D.	13/16	15/17	14/15	12/14	14/16
0600 GMT					
Mean	41/NA	45/NA	44/NA	42/NA	43/NA
S.D.	13/NA	16/NA	14/NA	13/NA	14/NA
1200 GMT					
Mean	44/45	47/49	49/49	48/57	47/50
S.D.	14/16	17/17	14/15	12/15	14/15
1800 GMT					
Mean	48/NA	48/NA	48/NA	50/NA	49/NA
S.D.	14/NA	15/NA	13/NA	11/NA	13/NA
0000 and 1200 GMT					
Mean	45/45	47/46	49/48	49/55	48/48
S.D.	13/16	16/17	14/15	12/14	14/16

points. On average the simulated MRH displays a diurnal range of 6% using these times of day, smaller in spring and summer.

The times of occurrence of maxima and minima merit consideration. It is expected that the diurnal mean relative humidity cycle is largely controlled by the diurnal temperature cycle, and only partially offset by an opposing diurnal cycle of surface evaporative fluxes. Thus, a morning humidity maximum and a late afternoon minimum are expected, similar to that shown by radiosonde observations. In the simulated humidities, however, the maximum is reached at 1800 GMT and the minimum is reached at 0600 GMT, on average. Further skepticism of the simulated humidity cycle is imposed by the fact that observed humidity increases by 3% between 0000 and 1200 GMT on average, whereas simulated humidity decreases by 1%. It appears that diurnal biases in cloud reporting may be contributing to biases in the simulated MRH.

Table 14 presents annual average changes of LFM MRH, simulated MRH, and radiosonde pseudo-MRH at various times of day. Presented in this manner, it is apparent that the simulated relative humidity fails to capture the diurnal cycle: the 0000 to 1200 GMT and 1200 to 0000 GMT changes are out of phase with that measured by radiosonde. Further, earlier speculation regarding the impact of cloudiness observation biases gains credence. The couplet between 0000 and 0600 GMT suggests that clouds were depicted well in the hours near and shortly after sunset (0000 GMT, by persistence) and again after sunrise (1200 GMT), but underestimated at night (0600 GMT). No dramatic couplets occurred during daytime.

Table 14 also shows that the LFM fails to capture the sense of the nocturnal humidity changes. Daytime changes appear to be handled adequately by the model, though this is likely a fortuitous consequence of the general temporal drying trend.

Table 14

Annual Average Relative Humidity Changes as a Function
Time of Day by Grid Points

	Radiosonde Pseudo MRH	LFM MRH	Simulated MRH
0000- 0600 GMT	1.6 linear estimate	-0.8	-4.7
0600- 1200 GMT	1.6 linear estimate	0.4	4.3
0000- 1200 GMT	3.1	-0.4	-0.4
1200- 1800 GMT	-1.3 linear estimate	-2.3	1.6
1800- 0000 GMT	-1.3 linear estimate	-1.5	-0.9
1200- 0000 GMT	-2.6	-3.8	0.7

Nevertheless, LFM humidities and humidity changes appear quite useful, once biases are removed, with 6-hr humidity change rms errors (not shown) averaging about 7% and 12-hour changes having rms errors averaging about 12%. Further, Table 15 suggests that the 18-24 hour humidity change forecast from the previous forecast cycle is virtually as reliable as the 6-12 hour forecast from the most recent cycle.

In conclusion, a study using frequent-interval radiosonde launches would shed light on the question of diurnal biases in the LFM humidities and in the simulated humidities. Simulated humidities have sufficiently low rms and mean errors that they appear to provide useful humidity information (Table 12), though diurnal biases exist (Table 13). Once these biases are removed, the simulated humidity changes also appear useful, with daytime root mean square errors (not shown) averaging about 11% in 6-hour changes and 14% in 12-hour changes.

2.3 Accuracy of patterns of LFM-II humidity forecasts

Much of this research remains to be done. Case studies show that frequently there are organized patterns of error positioned with respect to the weather regime. Sometimes these are related to misrepresentation of gradients or to errors in movement of weather systems. Techniques must be developed to identify and correct these situations.

In many situations the pattern of the LFM humidity forecast qualitatively seems representative of the large-scale humidity field, but without sufficient amplitude. Experiments should be conducted on the effects of inflating the variance of the LFM forecasts based upon the average ratio of the variances determined empirically, as presented in Section 2.1.

Some results of preliminary studies correlating LFM forecasts of humidity and humidity changes with satellite-measured brightness and brightness change

Table 15

Annual Mean and RMS Errors of MRH Changes

	LFM Mean Error	RMS Error
0 - 6 hr	linear estimate	NA
6 - 12 hr	linear estimate	estimate 7.2
0 - 12 hr	-3.8	11.8
12 - 18 hr	linear estimate	NA
18 - 24 hr	linear estimate	estimate 7.5
12 - 24 hr	-0.4	12.4

are presented in section 3.4. These tentatively indicate that brightness and LFM-forecasted mean relative humidity are highly correlated (up to correlation coefficient of 0.89) when cloud patterns are dominated by synoptic-scale systems and are less correlated under conditions of mesoscale and boundary-layer forcing.

3. DEVELOPMENT OF SATELLITE IMAGE-PROCESSING CAPABILITY

In order to incorporate satellite data into schemes for analysis of cloudiness and cloudiness change, it was necessary to develop an objective, automated image processing system. It was felt that such a system should perform three functions: (1) permit overlay of conventional meteorological objective analyses (in the form of isopleths) onto the satellite image for rapid comparison (on a video screen); (2) calculate average values of brightness or infrared flux for the set of grid points upon which the conventional objective analysis was performed, with averaging performed on a circular region of pixels centered on the grid points and with radius compatible with the resolution of the conventional data; (3) calculate histograms of the count values within each averaging circle, for the purpose of determining the nature and distribution of the clouds present. Computer programs have been completed to perform the first two tasks, and they are described below. Work on the third task is continuing.

Satellite imagery is received in real time at Penn State initially in analog form via C-5 conditioned telephone line from Washington, DC (the GOES-TAP network). Digital satellite data are obtained through conversion of the analog data, and can be displayed on a video monitor using a Grinnell Systems video displaying processor. This processor is also used in the tasks listed above.

Conventional meteorological data are received in real time at Penn State via the FAA (1200 baud) 604 circuit. Included on this circuit are hourly surface data, upper-air data, manually-digitized radar data, selected LFM analysis and forecast data for various stations, and model output statistics (MOS) data for various stations. These data are processed and archived using a Digital Equipment Corporation (DEC) PDP 11/34 computer system. Many analysis routines have been developed on this system, as described by Cahir et al. (1981) including cross-sections, time sections, soundings, and non-dimensionalized mappings. For comparison with satellite imagery, however, analyses of meteorological data are performed on quasi-horizontal analyses, with values calculated on a 30x40 grid referenced to a polar stereographic map background. A number of geographic regions are available as map backgrounds, but the "E" map (covering roughly the eastern half of the United States with a grid length of roughly 50 km) has been used exclusively in the imagery-comparison studies of sections 3.3, 3.4, 4.1, and 4.2.

3.1 Overlay capability for interactive comparison of spatial relations between cloudiness and potential predictor fields

In order to obtain a quick visual inspection of spatial relationships between cloud patterns and fields of conventional meteorological data, a program was developed to overlay conventional meteorological analyses onto satellite imagery. This program is run interactively in the following sequence.

1. The meteorologist runs a program to display an archived set of digital satellite data in video form, using the Grinnell system. Figure 2 is an example of such a display, from 1631 GMT on September 3, 1982.
2. The meteorologist decides which meteorological field (or fields) to overlay on this image, and runs a program to generate a gridded data



Figure 2 Photograph of the Grinnell television display of the visible satellite image at 1631 GMT on 3 September 1982. The box is movable by a cursor and is used for geographic registration of the image.

file of this field. The analysis program generates isopleths and locates points of maxima and minima of the field with respect to a polar stereographic map background, at intervals selected by the meteorologist. (Examples of such an analysis are given subsequently in Figures 6b, 7, 8, and 9.)

3. The operator begins running the overlay program and identifies which of the various satellite sectors has been displayed on the screen. The program responds by displaying some geographic reference points at locations where they typically occur on the screen relative to that sector.
4. If the reference points are not aligned properly on this image, the operator activates a cursor (as in Fig. 2) and identifies two reference points on the screen and specifies their latitudes and longitudes. The overlay program uses this information to calculate constants to correctly position and scale the meteorological field to be overlaid.
5. The operator identifies which analysis (or analyses) is to be displayed on the image. The overlay program then identifies the geographic position of the isopleths and points of maxima and minima, transforms these positions to screen coordinates, and displays the overlay field. Figure 3 is an example of the display after a meteorological field has been displayed over the 1831 GMT visible satellite image of August 28, 1982. In this case the overlay field is surface moisture divergence. (For future reference, in regard to section 4.2, the correlation between this brightness field and moisture divergence was near zero, the worst case of the study.)



Figure 3 Photograph of the Grinnell television display of the visible satellite image of 1831 GMT on 28 August 1982 with an overlay of surface moisture divergence.

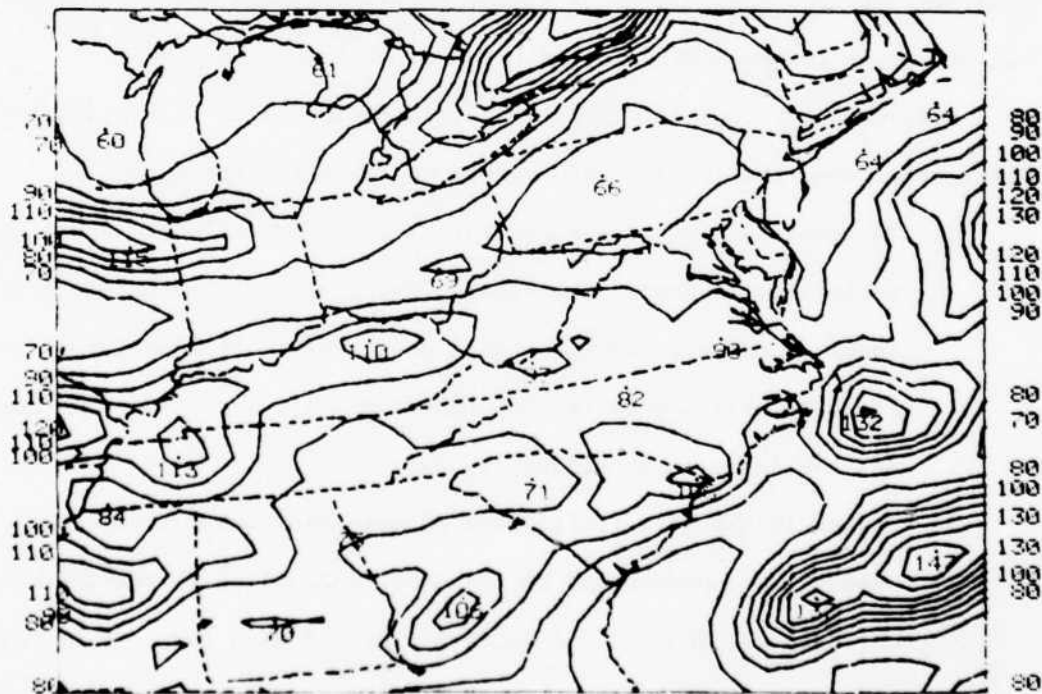


Figure 4 Average brightness of the satellite image of Fig. 3, calculated on 30x40 grid and displayed on a map.

3.2 Quantitative processing of imagery statistics

In order to establish quantitative, objective relationships between meteorological fields and satellite-inferred cloudiness or cloudiness change, a program was developed to calculate satellite imagery statistics in the vicinity of the grid points of the meteorological analyses. At present the program calculates average count (of brightness or infrared flux) in a meteorologist-specified radius around each grid point. (Reflectance can also be averaged, as described below.) When complete the program will also provide information about the distribution of counts within the averaging (or processing radius), for use in objective estimates of fractional cloudiness and cloud type.

The satellite statistics program incorporates many of the algorithms of the overlay program, specifically the interactive process of establishing reference points on the image. In this case the transformation algorithm locates each analysis grid point with respect to the satellite image and determines the number of pixels corresponding to the processing radius there.

Before performing the statistical calculations, the statistics program first makes some preliminary adjustments to the satellite data.

1. To remove any picture to picture variations in count values due to variations in phone line signal, the gray-scale reference strip of each image is compared to a standard gray scale. If departures from the standard exist, a correction factor is calculated for each count value and the image count values are adjusted.
2. Spikes in the data (introduced because geographic reference points are superimposed on the data transmitted on the GOES-TAP network) are removed. A spike is defined as a count 50 or more units greater than that of any of the 4 adjacent pixels. The anomalous count is replaced by the average count of the 4 adjacent pixels.

3. The counts are normalized to account for variations in solar zenith angle due to latitude, longitude, time of day, and day of year. Counts are normalized through correction of the value to that at zero zenith angle (sun overhead).
4. At the decision of the meteorologist, reflectances can be calculated³ from the visible count data (Muench, 1981),

$$r = a + (c/d)^2 \quad (2)$$

where r is reflectance, c is the count and a and d are constants.

Average brightness (or infrared flux) at a grid point is calculated from values at all pixels falling within the meteorologist-specified averaging radius. The average count is a weighted average, with weighting factors determined from

$$W = (D - R)/(D + R), \quad R < D \quad (3)$$

where D is the meteorologist-specified averaging radius and R is the radius of a particular pixel from the location of the grid point. Figure 4 is an analysis of the average brightness corresponding to Fig. 3.

In practice, average brightnesses have been calculated for two averaging radii, ~ 35 km and ~ 128 km. The latter is more consistent with the scale of conventional meteorological data. Figure 5 is an example of a visible satellite image with an overlay of average brightness (128 km radius) from 1631 GMT on September 3, 1982.

³The present averaging studies have been performed for the purpose of using the values in correlation studies, and average count values have been used. This choice was made because tests using count values and reflectances showed only slight differences (~ 0.01) in correlation coefficients, and computation time is reduced through elimination of computations of (2). The correlation coefficients are similar because application of (2) to a field of points does not appreciably change the pattern of the isopleths.

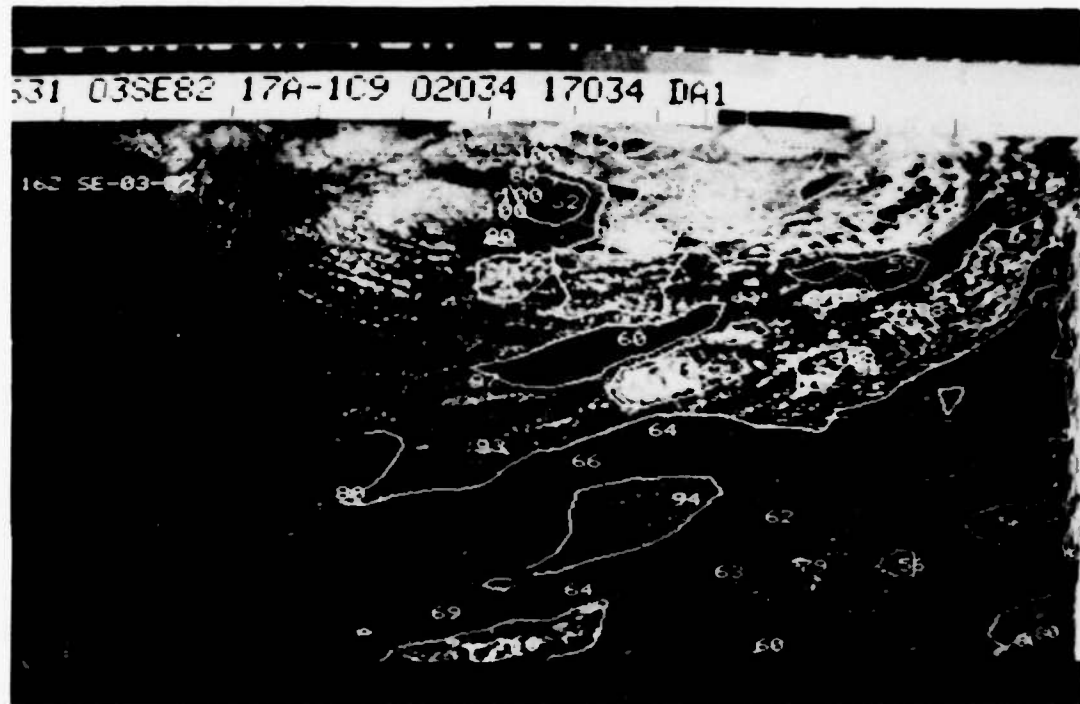


Figure 5 Photograph of the Grinnell television display of the visible satellite image of 1631 GMT on 3 September 1982, with an overlay of average brightness, with averaging radius 128 km.

These satellite-processing programs have been given a rather brief write-up, but the program development took many man-months of effort. These programs are, of course, available to AFGL. The following sections give some examples of the potential power of the system, which can be used operationally in real time.

3.3 Comparison of brightness and sub-synoptic scale, off-time simulated mean relative humidity

Section 2.2 described a scheme for using surface observations to estimate mean relative humidity in the lower troposphere (about 1000-500 mb). In that section it was shown that values of these simulated mean humidities were relatively accurate and unbiased estimates of radiosonde-derived mean humidities. One of the first uses of the method was to calculate values to use in studies of correlations of average brightness and simulated MRH.

Average brightness was used in this study instead of "I.R. temperature" because it provides a more unambiguous cloud/no cloud decision during the summer. Furthermore, recovery from enhancement of I.R. temperature is very difficult.

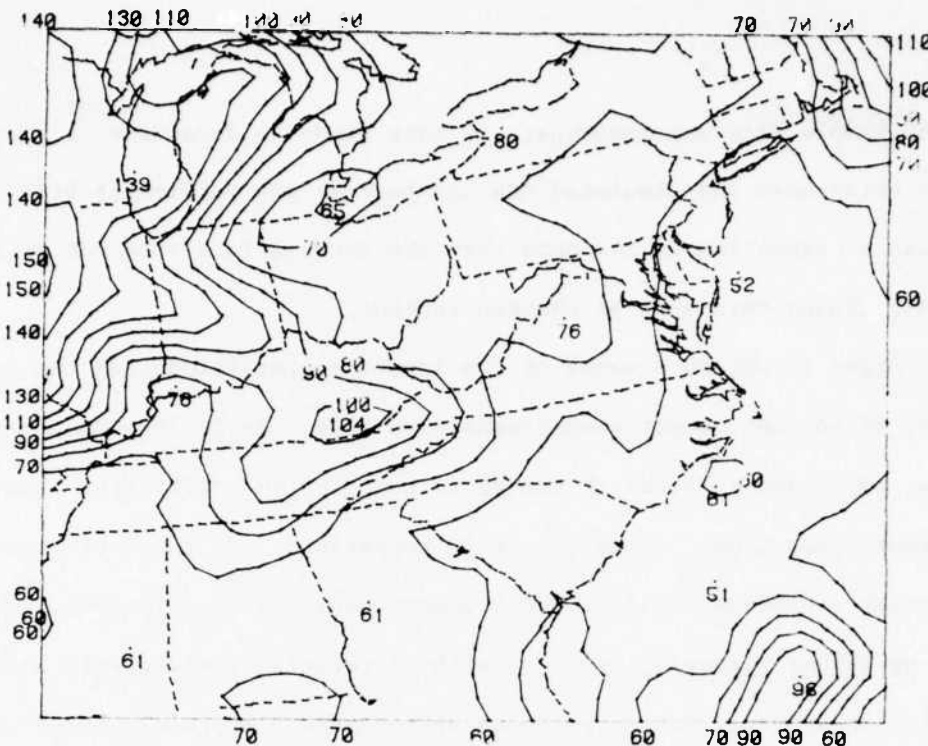
Brightness data were collected at one or more times of day on 18 days during August and September, 1982, over a region covering roughly the eastern half of the United States and a portion of the western Atlantic Ocean. Archived surface data were used to obtain fields of simulated humidities which were then compared with averaged brightnesses obtained from the satellite statistics program. A correlation program was developed to compare the values of average brightness and simulated MRH only at grid points where data existed in the immediate vicinity of the grid point (within a radius of 3 grid intervals for relatively small data gaps and within about 1.5 grid intervals for extensive data-void regions). For example, grid points over water bodies were eliminated

by this check. Correlations were based upon values at 913 to 996 grid points in this experiment.

Brightness fields were compared to simulated humidities at concurrent and displaced times. Further, average brightnesses were calculated at two averaging radii, 35 km and 128 km. The first test was to determine which of these radii resulted in the highest correlation coefficients. Of 33 direct comparisons, the large averaging radius was superior in every case. On average, however, the correlation coefficients were only slightly different (by 0.05). Apparently the simulated humidities are calculated on a scale that is somewhat too large to resolve the details of the small radius weighted-average brightness. Only correlations between simulated MRH and large-radius average brightnesses are discussed below.

Suitable visible imagery is generally available on the GOES-TAP circuit on the half hour. Surface data are collected roughly on the hour. Thus, there is a choice of comparing the $t - 1/2$ or $t + 1/2$ hour simulated MRH to the average brightness field as "concurrent" data. Of 9 comparisons of $t - 1/2$ and $t + 1/2$ hour correlation coefficients, the $t - 1/2$ hour simulated humidities showed larger correlation coefficients on 7, though average differences were small. Furthermore, there is reason to believe that the time correspondence is better at $t - 1/2$ hour as a result of observational practice. Hence, $t - 1/2$ hour simulated humidities are hereafter defined as the field for use as "concurrent" comparisons with average brightness.

Correlation coefficients were obtained for 19 concurrent comparisons of average brightness and simulated MRH, from various times on 9 days. The average correlation coefficient was 0.61, with a range from 0.44 to 0.86. Figure 6a presents mappings of average brightness ($r \approx 128$ km) and simulated MRH (Fig. 6b) at 1831 (180) GMT on August 24, 1982, the pair with the largest correlation.



41

Figure 6a Minicomputer analysis of brightness (128 km averaging radius) at 1831 GMT on 24 August 1982.

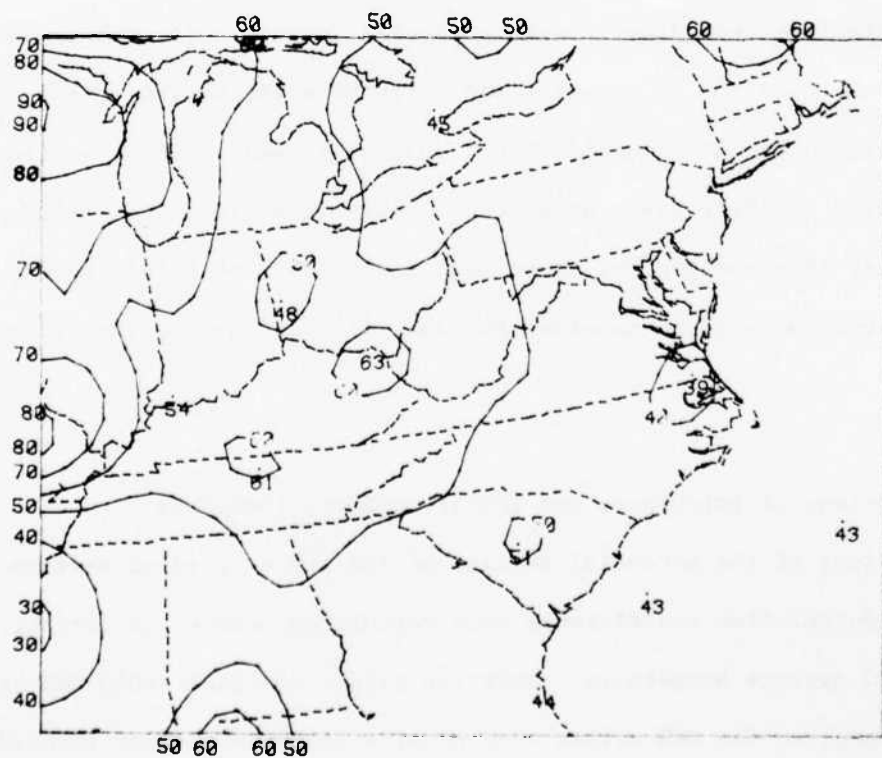


Figure 6b Minicomputer analysis of simulated mean relative humidity at 1800 GMT on 24 August 1982.

The sample size was inadequate in this study to determine if the correlation between brightness and simulated MRH was best at any particular time of day. There was a suggestion in the data that the correlations were not as large after 1800 GMT, though this must be checked further.

In order to obtain a sense of the impact of persistence on the correlations, a number of non-concurrent comparisons were made. Table 16 summarizes these results, expressed in terms of change in correlation coefficient from that of the concurrent comparison. In only 4 of 39 comparisons was the correlation coefficient increased, so concurrent comparisons are clearly best. Persistence showed up rather strongly, however, with correlation coefficients altered only slightly, on average, for comparisons up to about 5 hours displaced in time.

Additional tests are needed to define more precisely the impact of persistence. In particular, brightness changes must be correlated with changes in simulated humidities.

The simulated humidity studies presented in this section have largely addressed the question of humidity and brightness estimation on sub-synoptic scales, through use of simulated MRH. Just as it was shown in section 2.2 that the simulated humidity gave, on average, reliable estimates of values at radiosonde sites, this section has shown that the pattern of simulated MRH is also reliable, even on a scale considerably smaller than that of the radiosonde network.

3.4 Comparison of brightness and LFM-II humidity forecasts

As a test of the potential ability of the LFM to predict average brightness patterns, correlation coefficients were calculated between concurrent fields of LFM MRH and average brightness. Only the latest available 0000 GMT cycles of the LFM were used, so the MRH values were usually about an 18-hour forecast. LFM

Table 16

**Effect of Using Non-Concurrent Simulated MRH and
Average Brightness on Correlation Coefficients**

Time Displacement Between Simulated Humidity and Brightness ($t_{sim} - t_{brt}$)	Change in Correlation Coefficient with respect to Concurrent=0.61	# of improvements	# in sample
< -12 hours	-0.53	0	6
-9 to -12	-0.38	0	6
-6 to -9	-0.18	1	7
-3 to -6	-0.08	1	6
-1 to -3	-0.02	1	4
+1	-0.06	1	8
2 to 5	-0.09	1	9
Total		4	39

(note overlap)

data was not available in the Penn State archives for some cases and only satellite imagery within an hour of the times 1200, 1500, 1800, and 2100 GMT was used. These images were compared to MRH data output for 1200, 1800, and 0000 GMT and interpolated to 1500 and 2100 GMT.

Because of the above limitations imposed on the sample size, only 14 comparisons of brightness and LFM MRH were performed. Each comparison used 750-900 grid points. The average correlation coefficient was 0.56, with a range from 0.21 to 0.89.

Table 17 shows a breakdown of the correlation coefficients by time of day. The sample is too small to draw any firm conclusions, but there is a suggestion that correlations are better early in the day. Overall the LFM 13-21 hour forecasts show correlation coefficients which are comparable, on average, to those of simulated humidities based upon cloud observations. Hence, the LFM humidities exhibit some skill in pattern prediction, a question introduced in section 2.3. There are far too few comparisons (3), but the LFM MRH change showed a modest correlation with brightness changes (0.25).

Table 17

Correlation Between Average Brightness and LFM MRH
(for 750-900 grid points on 5 different days)

<u>Time</u>	<u>Avg. Correlation Coefficient</u>
1300, 1400, 1500, 1600 GMT	0.62
1700, 1800 GMT	0.52
2000, 2100 GMT	0.55
<hr/> Average	0.56

4. LOCAL FORCINGS AND INSTABILITIES

Studies are being performed to ascertain which potential predictor variables are useful for short-term forecasting of cloudiness and precipitation. This work is in its early stages and much remains to be learned. This chapter presents a few of the preliminary results.

4.1 Studies of potential predictors

Preliminary studies of potential predictors have used the summer, 1982 samples of brightness data obtained from the satellite statistics program. After inspecting the cases it became apparent that the sample was composed of a number of weather regimes. Most of the clouds were convective, but on some days the weather was dominated by synoptic scale systems, with clouds predominantly associated with fronts and comma cloud systems. Other days were dominated by "random" convection and organized mesoscale systems. Most days fell somewhere between these extremes.

The preliminary studies of potential predictors seem to indicate that different predictors are useful in different weather regimes. Table 18 was prepared to show the different performances of several potential predictors on a day judged to be dominated by synoptic-scale systems (September 1, 1982) versus a day dominated by convective processes (August 17, 1982). The potential predictors are grouped into three categories: those from LFM forecast data, those from observed data, and those from a mixture of observed and LFM forecast data.

The LFM predictors clearly show the difference in weather regimes: in every instance the LFM predictors are superior on the day with synoptic-scale forcing. Even the lifted index performs better on those days though the level of skill is low. Signs of the correlation coefficients are as expected in every instance except for the PBL V wind component on the convectively-forced day. Here a northerly wind had a slight tendency to be more cloudy than a southerly wind.

Table 18

Examples of Correlation Coefficients of Various Potential Predictors in Comparison with Brightness on Days of Different Weather Regime

Potential Predictor	GMT		Synoptic-Scale Forcing (9/1/82)	Convective Forcing (8/17/82)
	Time Predictor	Time Brightness		
LFM Predictors	LFM 18-h FCST MRH	1800/1800	0.85	0.21
	LFM 18-h FCST R1	1800/1800	0.73	0.16
	LFM 18-h FCST R2	1800/1800	0.80	0.34
	LFM 18-h FCST R3	1800/1800	0.52	0.00
	LFM 18-h FCST PBL Mixing Ratio	1800/1800	0.16	0.13
	LFM 18-h FCST Vertical Velocity	1800/1800	0.70	0.17
	LFM 18-h FCST PBL Divergence	1800/1800	-0.32	-0.17
	LFM 18-h FCST PBL Relative Vorticity	1800/1800	0.63	0.15
	LFM 18-h FCST Lifted Index	1800/1800	0.13	0.06
	LFM 18-h FCST PBL U Wind Component	1800/1800	0.32	0.14
	LFM 18-h FCST PBL V Wind Component	1800/1800	0.36	-0.07
	Advection of Obs. Potential Temp. by LFM 18-h Winds	1800/1800	0.25	-0.15
	Advection of Obs. Wet-bulb Potential Temp. by LFM 18-h Winds	1800/1800	0.37	-0.07
Observed Surface Fields	Potential Temp. Gradient	1800/1800	0.41	0.25
	Wet-bulb Potential Temp. Gradient	1800/1800	0.41	0.15
	Potential Temp. Wet-bulb Potential Temp.	1500/1800	-0.57	0.13
	Dew Point Temp.	1500/1800	-0.45	0.14
	Temperature	1500/1800	-0.41	0.10
	Dew Point Depression	1500/1800	-0.70	-0.12
	Moisture Divergence	1500/1800	-0.70	-0.33
Observed Upper-Air Fields	-w (Adiabatic Vert. Vel.)	1200/1500	0.28	0.11
	500 mb Vorticity Advection	1200/1500	-0.21	0.08
	500 mb Geostrophic Vorticity Advection	1200/1500	-0.13	-0.02
	K Index	1200/1800	0.24	0.31
	Totals Index	1200/1800	0.18	0.24

This may suggest that cold advection was allowing unstable boundary layers under partly sunny skies, but the correlation coefficient is so small that prolonged contemplation of this enigma is unjustified. The negative sign of the correlation coefficients for PBL divergence indicates that convergence (DIV<0) favors clouds, as expected.

The physical processes involved in the mixed predictors are discussed in some detail in Chapter 5. These terms represent advection of potential temperature, and relate to overrunning. Forecast PBL winds were used (rather than surface winds) in an attempt to require that overrunning occur in a layer of significant depth. Again the result was superior on the day of synoptic-scale forcing where overrunning of frontal zones was triggering (convective) clouds. On the day of convective forcing the correlation coefficients were nearly zero.

The predictors from observed data also indicate the difference between weather regimes. Large-scale vertical velocity, from the adiabatic vertical velocity equation

$$-\omega = -\vec{V}_r \cdot \nabla P_0 \quad , \quad (4)$$

where P_0 is the pressure of the isentropic surface and \vec{V}_r is the wind relative to the travelling weather system, shows larger correlations under conditions of synoptic forcing. So does horizontal moisture divergence,

$$\text{Moisture Divergence} = -\nabla_H \cdot (\vec{q} \vec{V}) \quad , \quad (5)$$

where q is the surface mixing ratio. Interestingly, the 500 mb geostrophic vorticity advection (calculated from geostrophic winds) and the 500 mb absolute

vorticity advection (calculated from observed winds) show near-zero correlation on the day of convective forcing and negative correlation coefficients on the day of synoptic-scale forcing. Apparently the synoptic-scale forcing was in the form of overrunning, and convective forcing was in the form of low-level destabilization (rather than mid-level cooling due to vertical motion).

Table 18 does suggest that heating increased cloudiness on days of convective forcing: there is positive correlation between initially warm, moist (θ , θ_w , T_D) areas and subsequent cloudiness only during the convective forcing regime. It is expected that the correlation would be improved if areas of initial cloudiness, contributing to development of relative cold spots, were eliminated. (This effect is discussed subsequently.) Indeed, on the day with synoptic forcing there is a substantial negative correlation, apparently due to persistence of clouds in overrunning regions.

Observed morning stability indices showed modest skill in predicting afternoon brightness patterns, superior to that of the LFM lifted index. Both the totals and K indices performed somewhat better on the day of convective forcing.

Several observationally-derived predictors appeared to be of value in both regimes, though better with synoptic forcing: dew point depression, and gradients of θ and θ_w . These predictors depict air that does not need much cooling (lifting) in order to saturate baroclinic regions where lifting is likely to occur.

Detailed studies of the September 1, 1982 case show that the relationship between initial potential temperature and subsequent brightness is extremely sensitive to initial brightness. That is, as suggested above, areas that are initially cloudy are also initially cool relative to adjacent sunny regions. If the cloudy regions are of sufficient size, owing to mesoscale or synoptic-scale organization, then there is a considerable persistence of brightness values at

most points interior and exterior to the cloud. Only a limited number of areas, especially near cloud edge, deviate from persistence. This persistence tendency contributes to a negative correlation between initial potential temperature and subsequent brightness.

When areas that were initially cloudy were eliminated from the comparison, the correlation coefficient on September 1, 1982 changed dramatically from the value of -0.57 obtained when all points were considered. The exact correlation coefficient obtained was quite sensitive to the value of brightness used as a cloud/no cloud threshold. On this occasion the correlation coefficient was most positive, about 0.7, in a range of brightnesses from about 70 to 80. Additional studies of this type are in progress.

4.2 Studies of surface moisture convergence and cloudiness

Many investigators have recognized the direct relationship between changes in column precipitable water and vertically-integrated horizontal moisture convergence. Further, other researchers have demonstrated that surface moisture convergence relates well to subsequent (1-6 hour) patterns of precipitation, especially of convective origin (Hudson, 1971; Anderson and Ucellini, 1974; Achtemeier and Morgan, 1975; Doswell, 1977; Ulanski and Garstang, 1978; Cunningham et al., 1982; Forbes et al., 1982; Park and Sikdar, 1982).

This section examines the relationship between surface moisture divergence and convergence and cloudiness and cloudiness change, as depicted by brightness, based upon the summer 1982 sample cases. Average brightnesses from the satellite statistics program have been used.

Table 19 shows average correlation coefficients for the relationship between surface moisture divergence at an individual hour and concurrent or subsequent

Table 19

Correlations Between Surface Moisture Divergence and Brightness,
Current and Subsequent

	Concurrent Brightness Correlation Coefficients	1-6 Hour Subsequent Brightness Correlation Coefficients
Average	-0.19	-0.25
Range	+0.08 → -0.423	-0.03 → -0.46
# Cases in Sample	13	20

average brightness. Large averaging radii were slightly better than small radii in each case and were used here. Correlations are slightly better for lag comparisons, as suggested by other researchers. Overall, the relationship was of the expected sign (32 of 33 comparisons) but the coefficients were modest.

Table 20 presents average correlation coefficients stratified by time of day whether comparing by time of analysis of moisture divergence or by time of the brightness analysis, there is a slight decline in correlation as the day progresses.

In order to attempt to eliminate transient noise in the wind data, time-averaged moisture divergences were also used. Time averaging was typically performed over a 4-6 hour period ending at the time of the brightness analysis used for comparison. This slightly improved the correlations over that from use of an individual hour, changing the average correlation coefficient to -0.29 from -0.20. Comparisons each typically involved more than 950 grid points.

These correlation coefficients are rather modest, on average. In part this is due to the fact that organized cloud systems, especially those of convective nature, develop an organized divergent outflow beneath cloud, with rather narrow convergent zones at the edges. Thus, many cloudy areas are divergent at the surface. This suggests that some regions should be eliminated from consideration, as was done with potential temperature (in section 4.1).

In view of the rather notable persistence of cloudiness patterns (correlation coefficients as large as 0.9 between brightness patterns 3 hours apart), however, short-term forecasting schemes must be judged on the basis of their ability to predict changes in cloudiness. Accordingly, the bulk of the preliminary experiments using surface moisture divergence have pertained to brightness change. Some of these experiments have limited the regions considered: areas of convergence were ignored where it was judged cloudy initially (as brightness

Table 20

**Correlation Between Moisture Divergence and Brightness
by Time of Day**

Stratified by Time of Analysis of Moisture Divergence		Stratified by Time of Comparison Average Brightness
<u>Times</u>	1200-1400 GMT	1300-1600 GMT
Avg. Corr. Coeff.	-0.29	-0.03
# Cases in Sample	7	9
<u>Times</u>	1500-1700 GMT	1700-1900 GMT
Avg. Corr. Coeff.	-0.26	-0.21
# Cases in Sample	13	15
<u>Times</u>	1800-2100 GMT	2000-2100 GMT
Avg. Corr. Coeff.	-0.16	-0.18
# Cases in Sample	11	9

would not likely increase) and areas of divergence were ignored where it was judged clear initially (as brightness would not likely decrease). The remaining domain of comparison evaluates the true meteorological value of surface moisture divergence in detecting clearing with divergence and increasing cloudiness with convergence.

Table 21 summarizes the results of preliminary experiments comparing surface moisture divergence and subsequent brightness change. Experiments were performed using both individual hourly moisture divergences and time-averaged moisture divergences, and in these experiments concerning brightness change it was found better to use the most recent individual hourly analysis of moisture divergence. Neither method showed any skill when all grid points were included, but once an approximate cloud/no cloud threshold was selected, correlations improved to respectable levels, -0.38 on average.

The predictive potential of surface moisture divergence, therefore, appears to be rather intimately related to the ability to specify the cloud/no-cloud brightness accurately. Experiments showed that this threshold brightness was fairly constant with time on any particular day, but varied somewhat from day to day (from brightnesses of roughly 85 to 110). Case studies suggest that this threshold is a function of weather regime (i.e. of cloud type and height), and can be reasonably estimated on a daily basis, and perhaps even by region of the analysis domain. When operational, the histogram section of the satellite statistics program (see section 3) is expected to contribute to this process.

4.3 Studies of precipitation and clouds along front-like boundaries.

Prior to the initiation of this contract, Forbes, Paone, and Cahir (1982) conducted objective experiments in forecasting mesoscale convection patterns using morning surface and upper-air analyses. The bulk of the skill of this

Table 21

**Correlations Between Surface Moisture Divergence and
Subsequent Brightness Change
Over Time Interval Varying from 3 to 7 Hours**

<u>Individual Hour Moisture Divergence</u>	<u>All Grid Points</u>	<u>Grid Points for Which a Physically Reasonable Change was Possible (brightness approx. 85-110)</u>
Average Correlation Coefficient	+0.05	-0.38
Range	+0.28 → -0.29	-0.23 → -0.57
<u>Time-Averaged Moisture Divergence</u>	<u>All Grid Points</u>	<u>Grid Points for Which a Physically Reasonable Change was Possible (brightness approx. 85-110)</u>
Average Correlation Coefficient	+0.08	-0.33
Range	+0.39 → -0.13	-0.15 → -0.47

scheme appears to be contributed by the use of surface moisture divergence multiplied by the Laplacian of the surface heating rate (as manifested by the 5-hour temperature change). This combined parameter was large and positive where there was surface moisture convergence at the warming side of a zone of heating gradient. Based upon data through 1500 GMT, this scheme gave accurate forecasts of 2135 GMT shower patterns.

For this project, a similar approach has been adopted to investigate night-time shower patterns. Under these circumstances mesoscale boundaries are not located by gradients of heating rate but by gradients of wet bulb potential temperature. The warm side of these boundaries are located objectively by the scheme of Cahir and Lottes (1982). Again, surface moisture convergence is involved. These studies, and those of chapter 5, serve to complement the largely daytime studies of chapter 3 and sections 4.1 and 4.2.

Surface moisture convergence alone can be a very useful diagnostic quantity for precipitation events, but it is also true that extensive regions of high humidity and cloudiness are associated with fronts. However, not all fronts are active. Thus, it is appropriate to consider frontal regions that are undergoing moisture convergence as being particularly susceptible to increases in humidity and cloudiness, and for production of strong precipitation from deep clouds. Accordingly, several case studies were performed to gain an idea about distribution of cloudiness/precipitation maxima along fronts, together with their evolution in time.

To accomplish this subtask, it was necessary to describe fronts objectively. Cahir and Lottes (1982) adapted such an objective technique from ideas first suggested by Clarke and Renard (1966). This involves calculating the absolute value of the gradient of the gradient of the horizontal temperature field, and then subjecting the field to a separate calculation of the sign of the associated

Laplacian. Negative Laplacian values are favored in warm air (temperature maxima) and help to differentiate the warm side of the gradient from the cold side.

In the present case, unlike Clarke and Renard, wet bulb potential temperature was used in order to emphasize the role of the moisture field at cloud-associated boundaries. Also, unlike them, this approach used hourly surface reports, with the aim of generating maps of potentially interesting boundaries hourly and at the best possible horizontal resolution. The resulting boundary-locator maps are applicable to something smaller than the synoptic scale, perhaps best described as the meso-a scale. It should be noted that the boundary-locator development was performed under a different Department of Defense Contract (ONR N00014-80-C-0945), and is simply being applied here.

It is convenient to combine the moisture convergence field and the boundary locator field mathematically prior to display. Interest lies in where the product of these two fields reaches a local (spatial) minimum, that is, where there is a large value of the (positive) gradient of gradient multiplying a negative and relatively large magnitude value of moisture divergence. This would correspond to strong local convergence along a wet bulb front. The requirement that the Laplacian of wet bulb potential temperature be negative does not affect the sign of the front locator, but does tend to eliminate minima in cooler air. Thus, most of these minima occur close to, and somewhat to the warm, moist side of wet bulb fronts. For convenience, we change the sign of these local minima, and call them maxima in a field that will be referred to as TRW.

Figure 7 depicts the mapping of the absolute value of the gradient of the gradient of θ_w , subject to the condition of a negative Laplacian (warm side) for 0000 GMT August 16, 1982. This field is the objective front locator, FNT. Also shown on Fig. 7 is the 0000 GMT position of the National Meteorological Center's

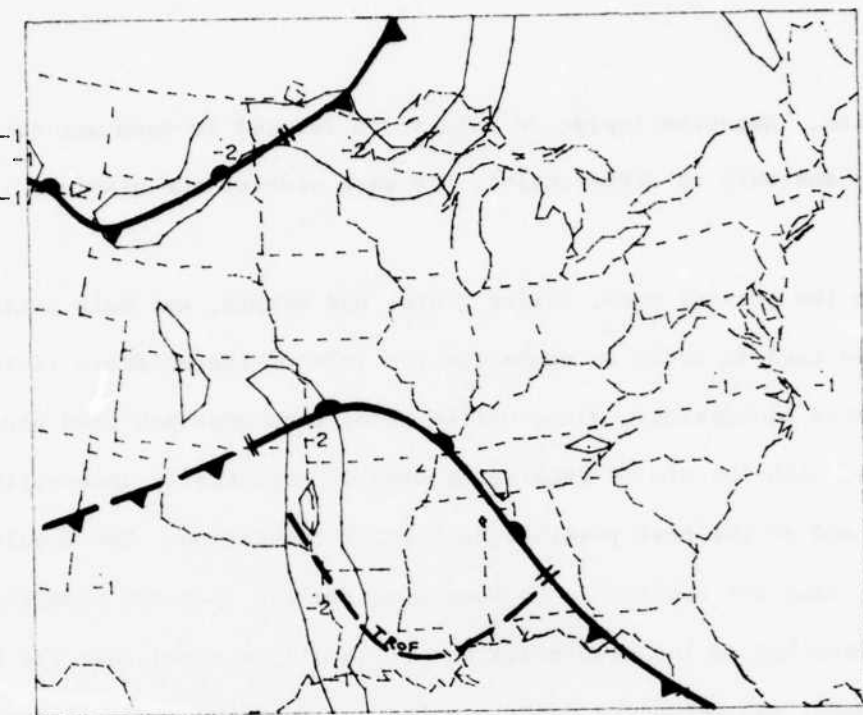


Figure 7 Mapping of the absolute value of the gradient of the gradient of surface wet bulb potential temperature, the objective front locator parameter, at 0000 GMT on 16 August 1982. Also shown are locations of fronts analyzed by the National Meteorological Center.

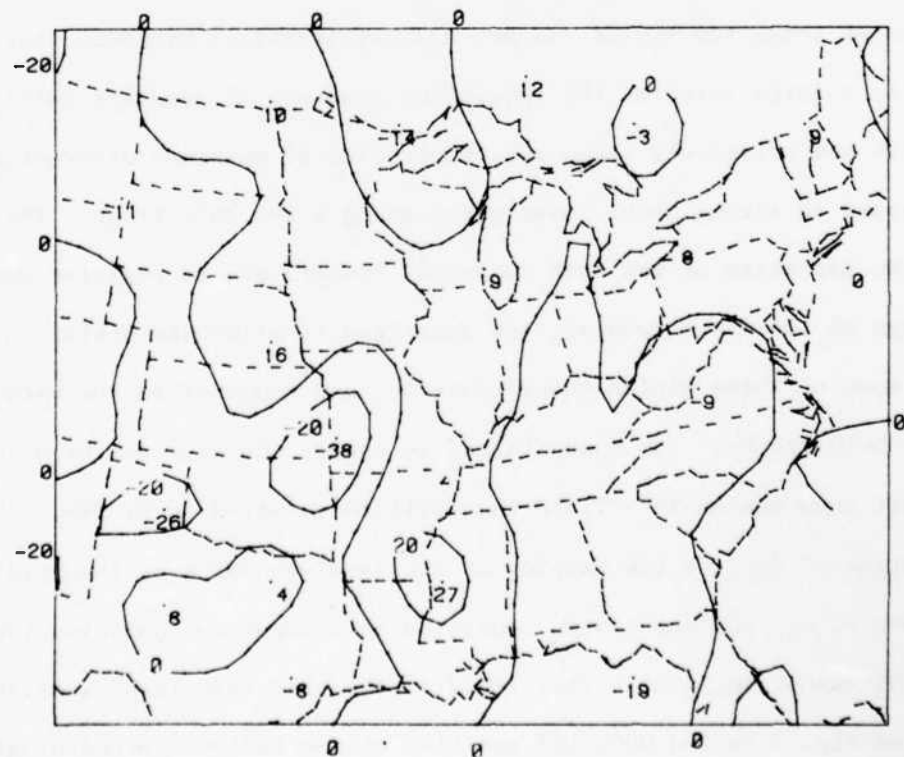


Figure 8 Minicomputer analysis of the surface moisture divergence (in units of $10^{-5} \text{ g kg}^{-1} \text{ sec}^{-1}$) at 0000 GMT on 16 August 1982.

(NMC) front analysis; there is little relation between them over the southern United States, but good agreement for the front in MN and the Dakotas. The boundary locator places a boundary along a nearly N-S line along the LA-TX, AR-OK, and MO-KS borders. This boundary is well away from, and oriented differently than the NMC fronts. Another boundary occurs in western KS-NE and still another through the southern Appalachians and AL. These other boundaries displayed some activity, with rains occurring in KY-TN, but this discussion focusses on the boundary that is not detected by conventional approaches, but which is very plain on Fig. 7.

The surface water vapor divergence for 0000 GMT 16 August is displayed on Fig. 8. The northern Plains front region was mildly convergent, with some divergence bridging across it. Weak convergence occurred over much of the Southeast, with a maximum amount along the NMC front position in the FL Panhandle. For the present discussion, the greatest significance lay in the strong moisture convergence near the northern end of the N-S boundary at the MO-KS border. Combining that field with the objectively calculated boundary locator, we find on Fig. 9 a very pronounced TRW maximum of 70 units. Note that this feature is very dominant on the map. Other minima occur, and are in most cases related to shower activity, but the MO-KS maximum calls for attention. In this event, heavy rain showers persisted in southern MO and AR throughout the night, producing precipitation amounts in excess of 5 cm. It appears that the TRW maximum in southern MO was related to that rain. In the following, the relationship between the TRW maximum and the associated rain is summarized for several cases.

Figure 10 depicts a schematic mapping of a mesoscale region of deep convective rain showers associated with a maximum in the combined moisture divergence and front locator fields, symbolized by the crossed circle, labeled

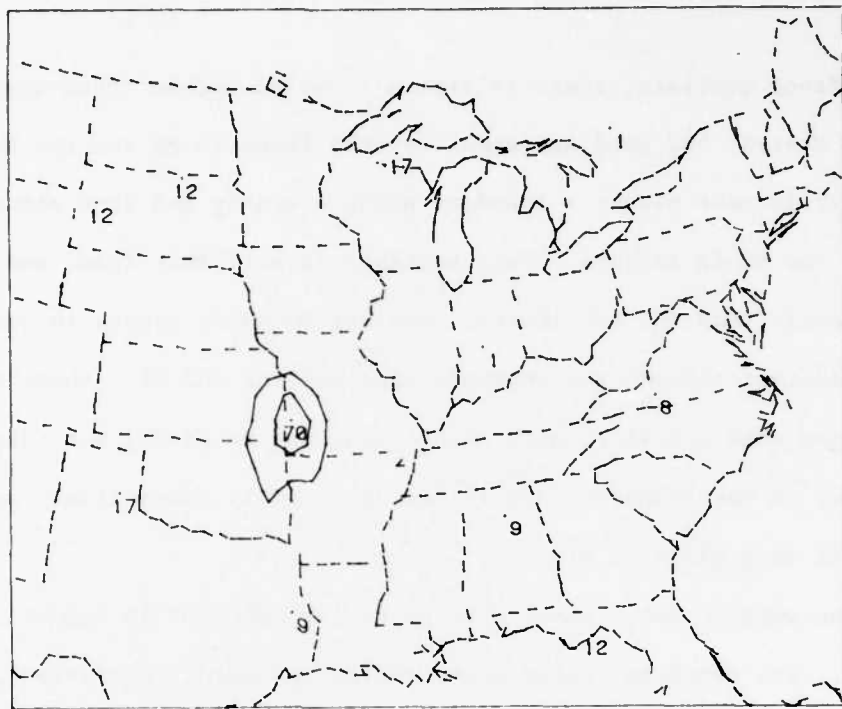


Figure 9 Display of the region where criteria are met satisfying the objective convection forecast parameter, TRW.

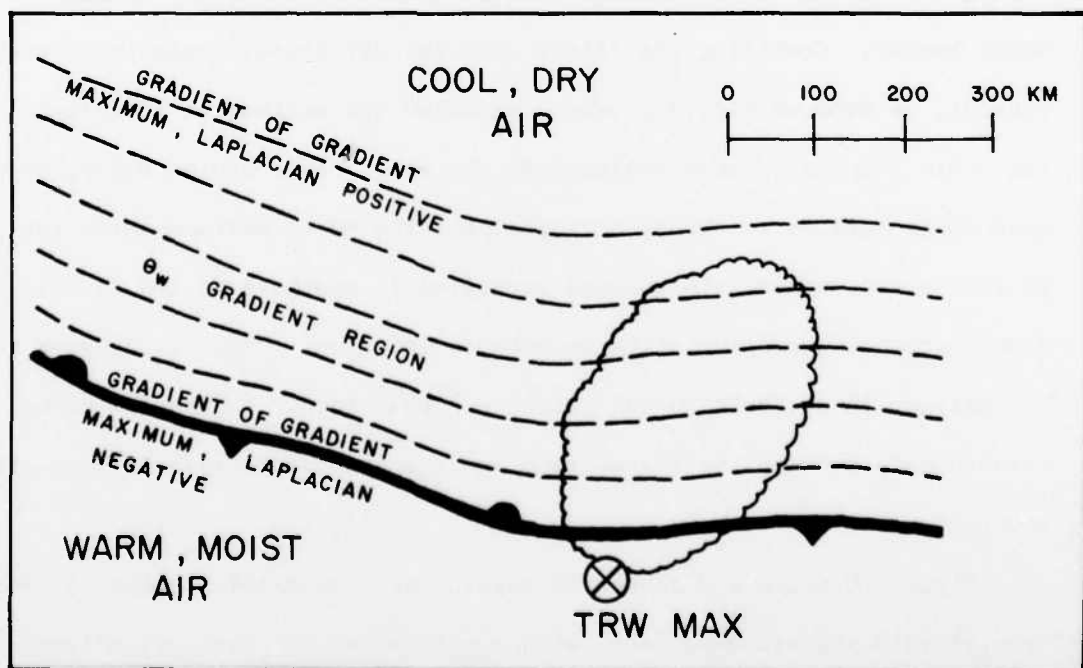


Figure 10 Schematic mapping of the mesoscale region of expected deep showers associated with surface moisture convergence near a front.

TRW. The maximum is usually slightly to the warm side of the objectively located front. Centered along the wet bulb potential temperature gradient vector is the associated region of enhanced cloudiness and showers, having a horizontal scale of 2 or 3 degrees latitude, that is, a mesoscale feature.

Although the night-time precipitation maximum is (as depicted by radar) usually found toward the cooler and drier air along the gradient vector through the maximum TRW point, there are variations in the angular relationship between the gradient vector through the maximum and the line to the center of the associated precipitation. However, once the precipitation pattern has formed, its center tends to remain at a fixed distance from the TRW maximum. This distance may range from 50 to 250 km. It varies little in individual cases. Of course, the TRW maximum point itself moves with time, but usually slowly and with very good time continuity. The conclusion is that the convection and the TRW maximum maintain a close, recognizable association over time.

Table 22 shows the magnitude of the TRW maximum, averaged over six August 1982 cases at various times in the late afternoon and night. It can be seen that the night-time weakening of the surface winds drops the TRW maximum from a higher daytime value of around 60 to a night-time value near 30 sometime between 0000 GMT and 0300 GMT. While the units themselves are somewhat arbitrary, depending as they do on grid length, the conclusion that the maximum sustains itself well enough to be easily located at night appears to have some promise, although this sample is too small for any firm conclusion.

The situation depicted applies to the night-time case where the boundary is acting in the sense of a convergent warm front or activated anafront. This normally implies low- and mid-level warm inflow into the so-called cold air. The term "so-called" is used to highlight the fact that this boundary can be a dew-point front in air that is very warm on both sides.

Table 22

Summary of TRW Maxima

<u>Time GMT</u>	<u>Mean</u>	<u>Standard Deviation</u>
2100	65	39
0000	64	39
0300	36	26
0600	30	11
0900	31	19

An alternative case arises when there is low-level cold advection in the cooler air. Then the mesoscale boundary behaves as a cold front and the enhanced shower feature is located on the warm side of the TRW maximum. At least in the warm seasons which have been studied so far, the warm front pattern, with the enhanced cloudiness and precipitation on the cold side of the boundary, is favored at night, while the cold front type is more common to the daylight or very early evening hours. The nighttime cases are often related to Mesoscale Convective Complexes (MCC) of the type discussed by Maddox (1980). In either event, the TRW maximum appears to be a useful diagnostic aid with implications for short-range prognosis.

4.4 Polar vortices as responses to flow instabilities

A somewhat different approach to short-term, mesoscale forecasting has been initiated by Forbes and Lottes (1982) under partial sponsorship by this contract. In this approach the mesoscale system (polar vortex) is observed in satellite imagery, and the future position of the system can be forecasted with reasonable accuracy based upon extrapolation and steering. Further, it is known that these mesoscale cloud systems evolve in a rather consistent way when they undergo development. The question addressed by the research is whether or not such development can be anticipated on the basis of observed data. The question can probably be re-stated as one of determining whether the development is in response to large-scale flow instabilities or whether development depends upon feedbacks internal to the mesoscale system, which would likely prevent forecasting of the development. Results of the research have already been reported by Forbes and Lottes (1982), so an extensive review is not given here. In summary, the study shows that there are several parameters which exhibit statistically significant differences between developing and non-developing systems in initial

stages of the system. These include initial cloud system configuration, areal extent, and depth; 500 mb temperature and average 1000-500 mb temperature; 700-500 mb lapse rate; 850 mb absolute vorticity; and windspeeds between 700 and 500 mb.

An obvious following step for these studies, and all of the studies of Chapter 4, is to develop regression equations combining miscellaneous predictors to form a short-term forecast. Naturally, this is planned. Though model output statistics (MOS) cloud forecasts (Carter and Glahn, 1976) also use regression equations, and display some skill (correlation coefficients of 0.3 to 0.6 depending on cloud amount category), the research for this contract will not be in competition with MOS. Emphasis here will be on the use of analysis of observed fields to predict short-term cloudiness and, especially, cloudiness change.

5. INTRA-SYSTEM FEEDBACKS

Because the atmosphere is a fluid, changes imposed upon the atmosphere in a local region (e.g. by mesoscale, topographic, or diabatic processes) are not necessarily confined to that region but can affect other portions of the weather system as well. The studies of section 4.3 illustrated this well, as nighttime moisture convergence in the warm sector apparently resulted in a current of air ascending along the slope of the anafront and producing convection above the frontal surface on the cool side relative to the surface position of the front.

Additional related studies of nighttime thunderstorms have shown that areas of positive advection of wet-bulb potential temperature by the 850 mb wind (near the top of the afternoon PBL) at 0000 GMT can be used to diagnose the occurrence and location of the convection. Again, convection occurs above anafronts, on the cold side relative to the surface front location. Studies are in progress to determine whether LFM forecasts of PBL winds can be used in this scheme. Several daytime results have been presented in Table 18 of section 4.1.

Figure 11 is a schematic diagram showing this process essentially in three dimensions. At the top, in horizontal view, a plume of air of high wet-bulb potential temperature is advected northeastward in the top of the PBL and rises over the stationary front surface. Convection occurs in the stippled region. The lower portion shows this flow in cross-section, with the air of high wet-bulb potential temperature hatched.

Research is in progress to examine the nocturnal nature of these activated anafronts in response to the diurnal heating cycle in the upstream warm sector. Observations show that a pool of air of high wet-bulb potential temperature forms in the warm sector somewhat displaced from the front (as depicted in Fig. 11) and is advected toward and over the front. The displacement between the highest wet bulb-potential temperatures and the front implies a certain transit time between

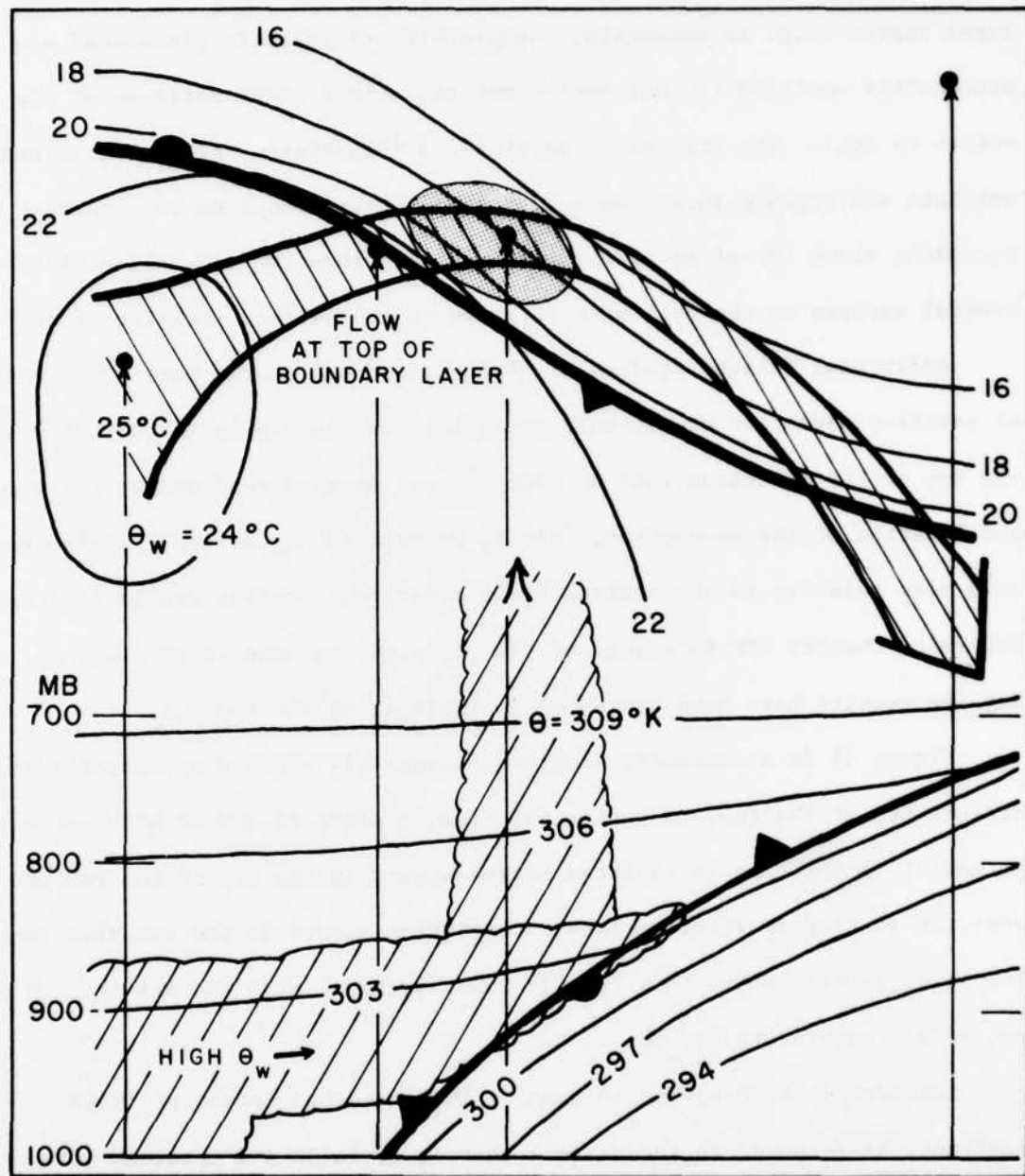


Figure 11 Schematic diagram showing the nature of the weather patterns conducive to nocturnal activated anafronts. At top is a horizontal mapping and at bottom a cross-section through the points indicated above.

these locations. The hypothesis is that the nocturnal nature of the frontal convection is a delayed response to upwind heating, the delay due to transit time. There may be some wind fluctuations contributing to the process also, but nocturnal overrunning convection would be favored for two reasons. First, the afternoon heated air (with higher θ_w) in the warm sector contains larger latent instability than at night. Second, daytime heating in the warm sector causes the adiabats to descend, whereas those above the frontal inversion are less likely to do so. This implies a potential for greater lift of this afternoon air during the subsequent period of transit.

A broader application of this type of approach could be in the study of the dramatic increase in cloudiness of weather systems as they first encounter inflow from regions with trajectories originating over adjacent warm water bodies. Many other feedback processes also can be studied.

6. PROSPECTUS FOR CONTINUED RESEARCH

As indicated in the introduction, the nature of humidity or cloudiness forecasting is one of assessing which of a number of scales or processes are contributing to the evolution of the weather. Accordingly, each of these contributing processes must be understood individually, and a decision tree must be invoked to apply the proper scheme to the situation. Project research will continue with a unifying theme: develop schemes for predicting short-term humidity and cloudiness change in the various weather regimes and develop a decision tree which enables the meteorologist to recognize the regime.

In each weather regime regression equations will be developed between predictors and changes in humidity or cloudiness. These studies will include evaluation of systematic LFM error patterns in relation to weather regimes.

One particular weather regime of interest is frontal cloudiness. Here several approaches are being investigated, as described above. The usefulness of VAS data to improve specification of front location and intensity will be investigated. Though the VAS soundings lack vertical resolution and contain much information that is redundant internally and with respect to other sources, it may be possible to extract data concerning horizontal temperature gradients of small scales from these soundings. VAS moisture information may also be of use in this project. Also related to moisture analyses, a set of special 3-hourly soundings has been obtained which were taken in connection with VAS experiments. The diurnal performance of simulated MRH will be tested using this data base.

In terms of frontal activity, two hypotheses will be investigated. One is that diurnal heating in the warm sector triggers nocturnal overrunning convection, as discussed in Chapter 5. The other hypothesis is that diurnal fluctuations in the winds cause the nocturnal precipitation maximum. Research on this hypothesis is a logical consequence of the studies of section 4.3, which

indicated that the boundaries behaved as warm fronts (activated anafronts) at night and as katafronts (cold fronts) during daytime. The theory is that a rapid increase of the flow of air in the warm sector toward and over the front, which produces the overrunning convection, is part of a frontal circulation induced by large-scale, relatively-rapid cooling of the dry air on the cold side of the front.

Acknowledgements

The authors appreciate the support of AFGL in funding this research. In addition to the authors, project research was also performed by Robert Scheinhartz and Gary Salamon.

References

Achtemeier, G.L. and G.F. Morgan, Jr., 1975: A short-term forecasting system: Step 1, Exploitation of the surface data. Preprints 9th Conf. Severe Local Storms, Norman, OK, Amer. Meteor. Soc., 18-24.

Anderson, C.L. and L.W. Uccellini, 1974: Studies of meteorological factors involved in the formation of severe local storms in the northeast Colorado region. Preprints, 8th Conf. Severe Local Storms, Denver, CO, Amer. Meteor. Soc., 84-89.

Cahir, J.J. and W.D. Lottes, 1982: An objective diagnostic aid in locating meteorologically significant boundaries. Preprints, 9th Conf. Wea. Forecasting and Anal., Seattle, WA, Amer. Meteor. Soc., 296-299.

Cahir, J.J., J.M. Norman and D.A. Lowry, 1981: Use of a real-time computer graphics system in analysis and forecasting. Mon. Wea. Rev., 109, 485-500.

Carter, G.M. and H.R. Glahn, 1976: Objective prediction of cloud amount based on model output statistics. Mon. Wea. Rev., 104, 1565-1572.

Clarke, L.C. and R.J. Renard, 1966: The U.S. Navy numerical frontal analysis scheme: further development and a limited evaluation. J. Appl. Meteor., 5, 764-777.

Cunning, J.B., R.L. Holle, P.T. Gannon and A.I. Watson, 1982: Convective evolution and merger in the FACE experimental area: mesoscale convection and boundary layer interactions. J. Appl. Meteor., 21, 953-967.

Doswell, C.A., 1977: Obtaining meteorologically significant surface divergence fields through the filtering property of objective analysis. Mon. Wea. Rev., 105, 885-892.

Forbes, G.S. and W.D. Lottes, 1982: Characteristics and evolution of mesoscale cloud vortices occurring in polar airstreams. Preprints, Conf. on Cloud Physics, Chicago, IL, Amer. Meteor. Soc., 310-313.

Forbes, G.S., T.A. Paone and J.J. Cahir, 1982: A minicomputer objective scheme for short-range forecasting of mesoscale convection patterns. Preprints, 12th Conf. Severe Local Storms, San Antonio, TX, Amer. Meteor. Soc., 84-87.

Fye, F.K., 1978: The AFGWC automated cloud analysis model. AFGWC Tech. Memo., 78-002, pp 31-43.

Hudson, H.R., 1971: On the relationship between horizontal moisture convergence and convective cloud formation. J. Appl. Meteor., 10, 755-762.

Kuo, H.L., 1965: On the formation and intensification of tropical cyclones through latent heat release by cumulus convection. J. Atmos. Sci., 22, 40-63.

Muench, H.S., 1981: Calibration of geosynchronous satellite video sensors. U.S. Air Force Geophysics Laboratory, Hanscom AFB, Environmental Res. Papers, No. 728, AFGL-TR-81-0050, 25 pp. AD A102894

Park, S.U. and D.N. Sikdar, 1982: Evolution of the dynamics and thermodynamics of a mesoscale convective system: A case study. Mon. Wea. Rev., 110, 1024-1040.

Ulanski, S.L. and M. Garstang, 1978: The role of surface divergence and vorticity in the life cycles of convective rainfall, Part I: Observations and analysis. J. Atmos. Sci., 35, 1047-1067.

DATE
ILME